People's Democratic Republic of Algeria

Ministry of Higher Education and Scientific Research

University of Echahid Hamma Lakhdar - El Oued

Faculty of Technology

Department of Process Engineering and Petrochemistry

Dissertation

ACADEMIC MASTER

Domain: Science and Technology

Specialty: Chemical Engineering

Presented by:

1. Chaima Fadhel
2. Afaf Tourqui

Entitled:

Engineering Ti-Modified Imogolite Nanotubes for Efficient Photocatalytic Hydrogen Production through Systematic Reaction Optimization

Publicly defended on: 14/06/2026

Board of Examiners:

Dr. Mohamed Yazid Belghith	**Chairman**
Dr. Khadidja Hadj Larbi	**Examiner**
Dr. Abdelatif Aouadi Université Paris-Saclay	**Supervisor**
Dr. Nader Shehata kuwait college of science and technology	**Supervisor**
Pr. Salah Eddine Laouini University of Echahid Hamma Lakhdar - El Oued	**Supervisor**

Academic Year: 2025/2026

الاهداء

بسم الله الرحمن الرحيم

{فَرِحِينَ بِمَا آتَاهُمُ اللَّهُ مِن فَضْلِهِ}

الحمد لله الذي وفقنا لإتمام هذا العمل المبارك الذي جاء تثمينًا لمجهودات مضت. الحمد لله أولاً وآخرًا فما تناهى دربٌ ولا خُتم جهدٌ إلا بفضله أما بعد:

أهدي بحث تخرجي بكل حب:

إلى نفسي أولاً التي رغم كل ما مررت به ظلت صامدة لتحقيق حلمي

إلى من كانت النور حين أظلمت دروبي والدافع في لحظات ضعفي واليد التي لم تخذلني أبدًا إلى أمي الغالية حفظها الله ورعاها

إلى نور عيوني وحبي الأبدي الذي آمن بي وبقدراتي وكان العون لي طول مسيرتي إلى أبي العزيز صاحب القلب الطيب حفظه الله ورعاه

إلى من تقاسموا معي لحظات التعب والسهر فكانوا خير معين لي أمان أيامي وضلعي الثابت إلى أخي وأخواتي

إلى من خطوت معها أولى الخطوات في مسيرتي الجامعية وواصلت معها إلى هنا فكانت خير أخت وصديقة إلى صديقتي العزيزة

إلى من كانوا سحبًا ممطرةً وأيادي ثابتة إلى كل صديقاتي

إلى العقول التي أنارت لي عتمة الجهل أساتذتي الأفاضل وإلى زملائي الذين كانوا خير رفاق في طريقٍ لم يكن ليخلو من التعب لولا وجودهم وإلى كل يدٍ مدت لي العون بصمت وكان لها أثر في هذا العمل.

اللهم تقبل مني هذا الجهد واجعله حجةً لي لا عليّ، وشاهداً بصدق السعي حين أُسأل عن شبابي فيما أفنيته.

عفاف تركي

الاهداء

بسم الله الرحمن الرحيم

{وَآخِرُ دَعْوَاهُمْ أَنِ الْحَمْدُ لِلَّهِ رَبِّ الْعَالَمِين}

الحمدُ لله الذي بنعمته تتم الصالحات، وبه تُختم الرحلات وتتحقق الامنيات.

اليوم لا أقف عند نهاية طريق، بل عند بداية حلم جديد.

سنوات مضت بين دراسة وتعب، بين سقوطٍ ونهوض، وبين حلم كبر معنا يومٍ بعد الآخر.

أهدي هذا العمل إلى:

والديّ الكريمين، من كانا لي السند والعون في كل خطوة، أدامكما الله لي وبارك في عمركما.

إخوتي الأعزاء، الذين كانوا مصدر دعمٍ وتشجيع دائم، لكم مني خالص المحبة والتقدير.

إلى صديقتي التي تقاسمت معي مشقة الطريق ولحظات التعب والنجاح

لكل من كان عوناً في هذا الطريق... للأصدقاء الاوفياء

ورفقاء السنين.

إلى أساتذتي ودكاترة الجامعة الأفاضل، الذين لم يبخلوا علينا بعلمهم وتوجيهاتهم القيمة ... جزاكم الله خيرا على كل ما قدمتموه.

اللهم علمني ما ينفعني وانفعني بما علمتني

وزدني علماً ولا تجعله آخر عهدي في النجاح.

الحمد لله قولاً وفعلاً وشكراً ورضا.

شيماء فاضل

الشكر والتقدير

شكر وعرفان

الحمد لله حمدا يليق بعظيم أسمائه، شكرا يليق بجميل الآئه والصلاة والسلام على نبينا محمد وعلى آله وصحبه أجمعين

قال رسول الله صلى الله عليه وسلم:" من لم يشكر الناس لم يشكر الله، ومن أسدى إليكم معروفا فكافئوه فإن لم تستطيعوا فأدعوا له"

ابتداءاً بهذا الحديث نتقدم بخالص الشكر والتقدير للدكتور المحترم" عوادي عبد اللطيف"، الذي لم يبخل علينا بعلمه وتوجيهاته، فكان لنا خير سند، جزاه الله عنا خير الجزاء

كما نتقدم بجزيل الشكر للدكاترة الأفاضل: الدكتور " لعويني صلاح الدين"، الدكتور" شحاته نادر" وإلى السيد عميد كلية التكنولوجيا وإلى كل أساتذة القسم الذين درسونا جزاهم الله كل خير

والشكر الموصول أيضا للقائمين على مخبر الدكتور لعويني على ما قدموه لنا طيلة تواجدنا به

نأمل أن نكون قد قدمنا عملا يكون بمثابة انطلاقة لأعمال أخرى تساهم في خدمة البحث العلمي

وفي الختام نشكر كل من ساهم من قريب أو بعيد في مساعدتنا على إنجاز هاته المذكرة ونخص بالذكر زملائنا في دفعة سنة ثانية ماستر هندسة كيميائية، متمنين للجميع دوام النجاح والتوفيق.

Abstract:

Achieving efficient photocatalytic hydrogen production requires not only advanced materials but also careful control of the reaction environment that governs charge transfer and surface reactions. In this study, this challenge was addressed through material engineering combined with systematic reaction optimization. Titanium-modified Imogolite nanotubes (Ti-Imogolite) were synthesized via a controlled hydrothermal method and evaluated for photocatalytic hydrogen production. Structural and spectroscopic analyses confirmed the successful incorporation of titanium into the Imogolite framework while preserving the nanotubular architecture. Optical measurements revealed a significant reduction in the band gap from 3.25 eV for pristine Imogolite to 2.24 eV for Ti-Imogolite, enabling improved light absorption and charge separation. A comprehensive optimization study of the reaction parameters including sacrificial agent type and concentration, irradiation conditions, lamp–reactor distance, and stirring speed—identified the key factors affecting hydrogen evolution. Under optimized conditions (10% TEOA, UV irradiation, 5 cm lamp distance, 900 rpm), Ti-Imogolite achieved a hydrogen evolution rate of 470µmol g^{-1} h^{-1}, nearly five times higher than of pristine Imogolite. Mechanistic studies suggested that photogenerated electrons play the dominant role hydrogen evolution process, while recycling tests indicated excellent catalytic stability.

Keywords: Imogolite Nanotubes (INTs), photocatalytic, hydrogen; Titanium.

Résumé :

La production efficace d'hydrogène par photocatalyse nécessite non seulement des matériaux avancés, mais aussi un contrôle intelligent de l'environnement réactionnel régissant le transfert de charge et les réactions de surface. Ici, nous relevons ce défi grâce à une stratégie combinée d'ingénierie des matériaux et d'optimisation systématique de la réaction. Des nanotubes d'Imogolite modifiés au titane (Ti-Imogolite) ont été synthétisés par une méthode hydrothermale contrôlée et évalués pour l'évolution photocatalytique de l'hydrogène. Des analyses structurales et spectroscopiques ont confirmé l'incorporation réussie du titane dans la structure de l'Imogolite tout en préservant son architecture nanotubulaire. Les mesures optiques ont révélé une réduction significative de la bande interdite, passant de 3,25 eV pour l'Imogolite vierge à 2,24 eV pour le Ti-Imogolite, permettant une meilleure capture de la lumière et un transport amélioré des charges. Une optimisation complète des paramètres de réaction — incluant le type et la concentration de l'agent sacrificiel, les conditions d'irradiation, la distance lampe-réacteur et la vitesse d'agitation — a permis d'identifier les facteurs clés contrôlant l'évolution de l'hydrogène. Dans des conditions optimisées (10 % de TEOA, irradiation UV, distance lampe de 5 cm, 900 tr/min), le Ti-Imogolite a atteint un taux d'évolution d'hydrogène de 470 µmol g^{-1} h^{-1}, soit près de cinq fois supérieur à celui de l'Imogolite vierge. Des études mécanistiques ont révélé que les électrons photogénérés dominent le processus d'évolution de l'hydrogène, tandis que des tests de recyclage ont confirmé une excellente stabilité catalytique.

Mots-clés: Nanotubes d'imogolite, Photocatalyse, Hydrogène, Titane.

الملخص:

يتطلب تحقيق إنتاج فعال للهيدروجين بالتحفيز الضوئي ليس فقط مواد متقدمة، بل أيضاً التحكم الذكي في بيئة التفاعل التي تحكم انتقال الشحنة والتفاعلات السطحية. في هذا البحث، نعالج هذا التحدي من خلال استراتيجية مشتركة تجمع بين هندسة المواد وتحسين منهجي للتفاعل. تم تصنيع أنابيب الإيموغوليت المعدلة بالتيتانيوم (إيموغوليت–تيتانيوم) باستخدام طريقة حرارية مائية محكمة، وتم تقييمها لإنتاج الهيدروجين بالتحفيز الضوئي. أكدت التحليلات الهيكلية والطيفية نجاح دمج التيتانيوم ضمن إطار الإيموغوليت مع الحفاظ على بنية الأنابيب النانوية. أظهرت القياسات الضوئية انخفاضاً كبيراً في فجوة الطاقة من 3.25 إلكترون فولت للإيموغوليت النقي إلى 2.24 إلكترون فولت للإيموغوليت–تيتانيوم، مما أتاح تحسين جمع الضوء ونقل الشحنة. حددت عملية تحسين شاملة لمتغيرات التفاعل—بما في ذلك نوع وتركيز العامل التضحي، وظروف الإشعاع، والمسافة بين المصباح والمفاعل، وسرعة التحريك—العوامل الرئيسية التي تتحكم في تطور الهيدروجين. تحت الظروف المثلى، (10% TEOA، إشعاع فوق بنفسجي، مسافة مصباح 5 سم، سرعة تحريك 900 دورة في الدقيقة)، حقق إيموغوليت–تيتانيوم معدل إنتاج هيدروجين بلغ 470 ميكرو مول لكل غرام في الساعة، أي ما يقارب خمسة أضعاف الإيموغوليت النقي. كشفت الدراسات الآلية أن الإلكترونات المتولدة ضوئياً تهيمن على عملية إنتاج الهيدروجين، بينما أكدت اختبارات إعادة الاستخدام ثباتاً ممتازاً للمحفز.

الكلمات المفتاحية: أنابيب الإيموغوليت، التحفيز الضوئي، إنتاج الهيدروجين، التيتانيوم.

TABLE OF CONTENTS

TABLE OF CONTENTS

List of Equations

List of Tables

List of Figures

GENERAL INTRODUCTION

General Introduction

Increasing global energy demand, coupled with the urgent need to mitigate environmental degradation and greenhouse gas emissions, has intensified the search for sustainable and clean energy alternatives. Among the various candidates, hydrogen has emerged as a highly promising energy carrier due to its high gravimetric energy density and environmentally benign use combustion, producing only water as a byproduct [1, 2]. In particular, green hydrogen, generated from renewable resources, represents a cornerstone in the transition toward a carbon-neutral energy economy [3].

Conventional hydrogen production methods, such as steam methane reforming and coal gasification, remain dominant on an industrial scale but are associated with significant carbon emissions and environmental concerns [4]. Although water electrolysis offers a cleaner alternative, its large-scale implementation is still hindered by high energy consumption, reliance on expensive catalysts, and the intermittent nature of renewable electricity sources [5]. These limitations have stimulated growing interest in alternative hydrogen production routes that can operate under milder conditions with improved energy efficiency.

Photocatalytic water splitting has emerged as a promising approach for direct solar-to-hydrogen conversion, offering the potential to harness abundant solar energy to drive chemical reactions without requiring external electrical input [6]. This process relies on semiconductor materials capable of absorbing photons to generate electron–hole pairs, which subsequently participate in redox reactions leading to hydrogen and oxygen evolution [7]. Despite its conceptual simplicity, the practical implementation of photocatalytic hydrogen production remains limited by several intrinsic limitations, including rapid charge recombination, limited light absorption, and insufficient catalytic activity [8].

Advances in nanotechnology have significantly contributed to addressing these challenges by enabling the design of materials with tailored electronic structures, high surface areas, and enhanced charge transport properties [9]. In this context, low-dimensional nanostructures materials have attracted particular attention due to their unique physicochemical characteristics,

which can facilitate efficient charge separation and provide abundant active sites for catalytic reactions [10].

Among these nanostructured materials, Imogolite nanotubes have recently gained considerable interest as a novel class of one-dimensional inorganic nanomaterials. Their well-defined tubular morphology, high aspect ratio, and intrinsic surface polarization make them attractive candidates for photocatalytic applications [11]. However, pristine Imogolite typically exhibits a wide band gap and limited visible-light absorption, which restrict its photocatalytic efficiency under solar irradiation.

To overcome these limitations, various modification strategies have been explored, including heteroatom doping, surface functionalization, and composite formation. In particular, the incorporation of transition metal species has proven to be an effective approach to modulate the electronic structure, enhance charge separation, and improve overall photocatalytic performance [12]. Titanium, owing to its favorable electronic configuration and well-established role in photocatalysis, represents a promising dopant for engineering the properties of Imogolite-based systems.

In this dissertation, we will specifically address the engineering of titanium-modified imogolite nanotubes for highly efficient hydrogen production through systematic reaction optimizing. Ti-Imogolite nanotubes were synthesized using a controlled hydrothermal method, followed by an evaluation of hydrogen production via photocatalysis.

This work consists of two parts: theoretical and practical:

The theoretical part contains three chapters:

The first chapter is a study on Imogolite, including its history, definition, composition, modifications made to it, as well as its applications. The second chapter discusses the characterization techniques used in this research, where each technique is defined along with its principle, and a photograph of the device is provided. These techniques, in order, are UV-Vis spectroscopy, Fourier-transform infrared spectroscopy, X-ray diffraction, X-ray fluorescence spectroscopy, and scanning electron microscopy. The third chapter covers hydrogen production by photocatalysis, including its history, methods used, types of materials employed, and a discussion of the advantages and disadvantages.

The experimental part contains two chapters:

The first chapter presents the materials and methods used in the fabrication of titanium-modified Imogolite nanotubes for hydrogen production by photocatalysis. The second chapter presents the results and discussion of the physical and chemical properties, the study of the success of titanium incorporation within the Imogolite compound, as well as the results and discussions on the efficiency of hydrogen production through this compound. It also covers the optimal sacrificial agent and its concentration, the distance between the lamp and the reactor, and the stirring speed.

THEORETICAL PART

CHAPTER ONE: IMOGOLITE

I-1 Introduction

Imogolite is a natural nanomaterial belonging to the hydrated aluminosilicate family. It was first discovered in volcanic ash soils in Japan in the 1960s, which has since attracted significant attention from materials scientists and soil researchers [13]. This mineral exhibits a hollow single-walled nanotubular morphology with an external diameter between 1.7 and 2.5 nanometers and an internal diameter less than 1 nanometer, which gives it unique surface and chemical properties [14]. Imogolite mainly consists of an aluminum octahedral layer bonded with hydroxyls and silicate tetrahedral layers, which provides structural stability and a high capacity for interaction with different molecules [15]. Moreover, this unique structure makes it very reactive to various physical and chemical modifications either by surface functionalization or intercalation of other species that can directly modify its properties and functions directly [16]. Because of these unique properties, Imogolite has been recognized as a potential candidate material in several modern applications, particularly in fields such as photocatalysis, adsorption of contaminants, and energy storage [17]. In this chapter, we will discuss the history and occurrence of Imogolite, its definition and chemical structure, modifications that it undergoes, and the most important applications related to various fields of science and technology.

I-2 History of Imogolites

Imogolite, a fine fibrous aluminosilicate clay particle, was initially discovered in Japan in 1962 (Yoshinaga and Aomine, 1962) [18]. Since then, they have been found worldwide as a common component of soils fromed either in weathered pyroclastic deposits or in volcanic ash. In the ten years after their discovery, its structure remained unclear despite numerous investigations. The initial structural models included several chains of AlO_6 octahedra connected sideways by SiO_4 tetrahedra and paracrystalline order (Wada, 1967; Wada and Yoshinaga, 1969; Russell et al., 1969) [13, 19]. The identification of an Imogolite fiber's morphology using high resolution electron microscopy in 1970 was a significant turning point (Wada et al., 1970) [14]. According to Wada et al. (1970), the fiber unit seen in micrographs is a hollow tube with an exterior diameter of 1.7–2.1 nm and an inner diameter of 0.7–1 nm. In a seminal paper, Cradwick

et al. (1972) offered a structural model explaining this tubular shape two years later. $Al_2SiO_7H_4$ is determined to be the nominal composition of Imogolite nanotubes (INT) [20, 21].

I-3 Definition

Imogolite is a natural nanoscale mineral composed of hydrated aluminosilicates, primarily found in volcanic soils, especially in volcanic ash soils. It features a unique structure consisting of one-dimensional single-walled hollow nanotubes with uniform diameters: an outer diameter of about 2 nanometers and an inner diameter of about 1 nanometer [14] whereas the inner surface contains silanol groups (Si–OH) resulting from the tetrahedral arrangement of silicon surfaces facing inward [22]. This variation in surface composition gives Imogolite distinctive chemical properties compared with other clay minerals [23]. Its approximate chemical formula is expressed as $(OH)_3\ Al_2\ O_3\ Si(OH)$ [24], making Imogolite one of the most prominent natural nanomaterials with promising applications in adsorption and catalysis.

I-4 Structure

Imogolite is a naturally occurring hydrous aluminosilicate that features a rolled structure similar to gibbsite, consisting of Al–OH octahedr on the outside and silanol (Si–OH) tetrahedra pointing toward the center [25, 26]. The inner orthosilicate anions (O_3SiOH) connect three oxygen atoms across the octahedral layer, which creates a structural stress due to the bond length difference between the shorter Si–O bonds (1.6 Å) and Al–O bonds (1.9 Å), leading to a curved shape of the Imogolite structure[26, 27]. Consequently, Imogolite is formed as long, thin, and hollow nanotubes that are hollow and have a recurring chemical formula of $Al_2SiO_3(OH)_4$.

It is formed naturally through the weathering of volcanic glass in soils derived from volcanic activity, with formation occurring primarily in well-drained, mildly acidic conditions (pH 5–7) or within volcanic ash deposits that experience low-temperature snowmelts [28]. Rainwater and snowmelt play a crucial role in the development of Imogolite as they help leach silica and alumina from volcanic materials [29], resulting in the creation of monosilicic acid that reacts with aluminum ions, which gradually converts amorphous precursors into Imogolite [26].

The lengths of Imogolite nanotubes varies from 100 nm to several micrometers, with cavity diameters of around 1 nm and outer diameters ranging from 2 to 2.7 nm [26]. Because Imogolite has octahedral surfaces composed of Al–OH groups and tetrahedral inner structures made up of Si–OH tetrahedrons, the presence of OH groups on both outer and inner surfaces enhances its hydrophilicity, providing sites for potential functional modification [30]. Nevertheless, the curvature of Imogolite influences the alignment of surface OH groups, which affects their ability to form hydrogen bonds with other functional groups in the molecule [25]. Consequently, water adsorption is more favorable in the Imogolite's inner cavity, where inner Si–OH groups are easily accessible for hydrogen bonding, allowing water molecules to fill the central cavity. This property grants Imogolite significant potential in water-related applications, ranging from reverse osmotic filtration[31, 32] to scaffolding development [33, 34] due to the increased water absorption and water flow when Imogolite is incorporated into the system.[34, 35]

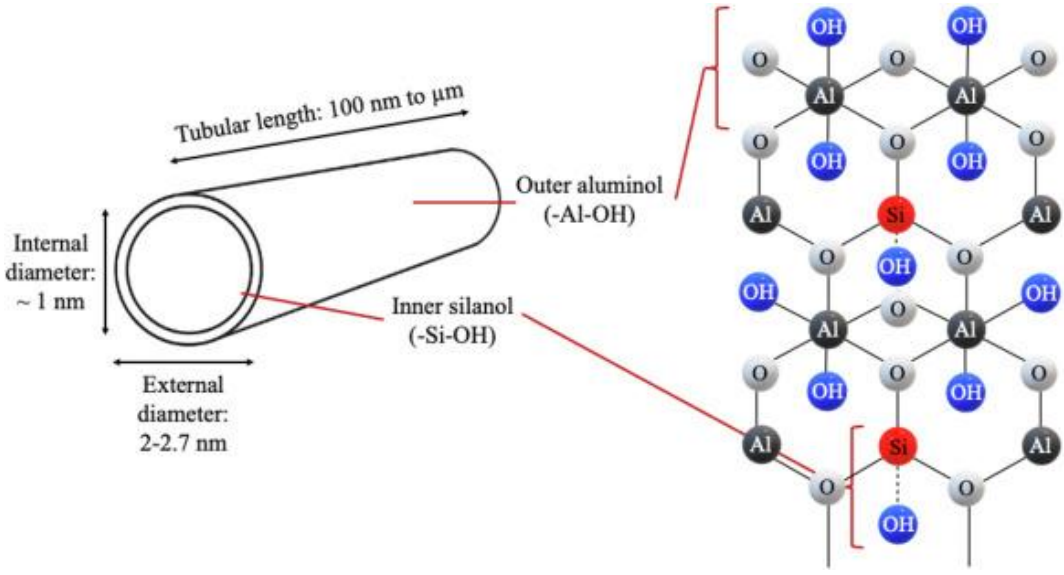

Figure (I-1): The hollow nanotube form of Imogolite consists of an outer aluminol (Al–OH) octahedron and an inner silanol (Si–OH) tetrahedron. [35]

I-5 Modifications

The major alterations or modifications done on Imogolite can be summarized as follows:

I-5-1 Changing the outer surface from hydrophilic to hydrophobic behavior

The exterior surface of Imogolite was modified by incorporating long-chain phosphate compounds such as dodecylphosphate, which resulted in an increase in the water contact angle from 22° to 93°. This indicates that the Imogolite transitioned from a hydrophilic material to a hydrophobic material. [36]

I-5-2 Grafting polymer chains onto the outer surface

A polymerization starter was attached to the surface of the Imogolite, after which poly(methyl methacrylate) (PMMA) chains were grown on top of it. This made it easier for the Imogolite to mix in organic liquids like THF, chloroform, and toluene, while pristine Imogolite could not dissolve in them. [36]

I-5-3 Altering the chemical environment within the tube

Bifunctional Imgolith was prepared internally utilizing diverse organosilanes; the tube's diameter remained unchanged, however, the polarity and reactivity inside the inner cavity changed significantly. [36]

I-5-4 Surface modification internally through organic silanes

Researchers mentioned that replacing internal Si–OH groups with trimethylsilyl compounds causes a slight decrease in the Young's modulus to increase electronic band gap of the Imogolite compared to the initial material. [37]

I-5-5 Removing internal hydroxyl groups through thermal treatment

The researchers clarified that heating to eliminate internal Si–OH groups causes Young's modulus to rise from 324 to 371 GPa, and the electronic band gap decreases from 9.1 eV to nearly 4.4 eV, which might convert Imogolite to a semiconducting material. [37]

I-6 Applications

I-6-1 Molecular Separation and Gas Adsorption

Imogolite's capacity to adsorb gases like carbon dioxide, methane, and ammonia within its nanoscale channels makes it valuable for applications in gas separation and the purification of air or natural gas. Furthermore, the selectivity of CO_2 separation from CH_4 or N_2 can be enhanced through modifications to the internal surfaces of these tubes. [38]

I-6-2 Filtration and purification of water

Imogolite can be utilized in membranes for water filtration because it can let water flow through its nanometer-sized channels while capturing some other molecules. The water flow rate has been found to increase when Imogolite is added to thin membranes. [38]

I-6-3 Polymer reinforcement and composite materials manufacturing

Imogolite is added to polymers such as polyvinyl alcohol (PVA) to make the material more rigid,

transparent, and resistant. Therefore, it is used in the manufacture of films, fibers, and advanced plastic materials.[38]

I-6-4 Drug Delivery and Medical Applications

Because the tubes can hold medications or biomolecules and release them gradually, Imogolite can be employed as a carrier for the gradual release of these substances inside the body. [38]

I-6-5 Photocatalysis and Chemistry

After being modified with elements like iron or titanium, Imogolite can function as a catalytic material or as a substrate for catalysts. These modifications make Imogolite suitable for photocatalytic reactions like the production of hydrogen or the removal of pollutants. [38]

I-6-6 Contaminant and Pesticide Adsorption

Imogolite is suggested for application in environmental remediation as it can soak up certain pesticides and organic pollutants from soil or water. It proves quite helpful in capturing herbicides, based on research. [38]

I-7 Conclusion

This chapter concludes that Imogolite is a rare clay mineral with a unique tubular nanostructure, differentiating it from other clay minerals. Its definition and distinctive structure were presented, as well as the main transformations that could occur on it under environmental conditions. It was also demonstrated that this mineral has potential applications due to its particular surface properties in the fields of water treatment, adsorption, and nanomaterials. Overall, Imogolite is an increasing scientifically important substance with potential application perspectives within material science.

CHAPTER TWO: CHARACTERIZATION TECHNIQUES

II-1 Introduction

Characterization techniques are a fundamental pillar in materials science; they enable the determination of the physical, chemical, and structural properties of the material and link them to its practical performance [39]. These techniques vary to include X-ray diffraction (XRD) for determining the crystal structure [40], spectroscopic analysis (FTIR) for exploring chemical bonds [41], and (UV-Vis) technique for studying optical properties and the energy gap [42]. Scanning electron microscopy (SEM) is important in examining surface and nanoscale structures [43], while (XRF) technology is employed to accurately determine elemental composition [44]. The synergy of these tools provides researchers with a comprehensive vision for developing modern and innovative materials.

In this chapter, we will address the theoretical foundations and scientific concepts upon which the most important material characterization methods are built; the review will cover (UV-Vis), (FTIR), (XRD) techniques, and the (XRF) method alongside the electron microscope (SEM). In each, we will strive to explain the physical principles and governing laws that justify the interaction of energy with matter, clarifying their operation from a scientific perspective that explains how results are derived. To complete the mental picture, illustrative images of each device will be attached, showing the essential components and main components of the instruments, granting us a deeper understanding of the principles that make these tools a precise means to comprehend the structure and properties of materials.

II-2 Ultraviolet-Visible Spectroscopy (UV-Vis)

Ultraviolet–visible (UV–Vis) spectroscopy is employed to obtain absorbance spectra of a substance in solution or solid form. The measured signal is the absorbance of light energy or electromagnetic radiation, which promotes electrons from the ground state to the excited state of the compound or material. The UV-Vis region for the electromagnetic spectrum covers 1.5 to 6.2 eV, which corresponds to a wavelength range of 800 to 200 nm. were studied using UV transmittance spectroscopy using the Shimadzu 3101PC double beam spectrophotometer [45].

II-2-1 Principle

UV-visible absorption spectrometry relies on the transition of valence electrons that move from a ground state to an excited state after absorbing a photon in the UV-Vis range .The principle of the UV spectrophotometer adheres to the Beer-Lambert law .This law states that when a monochromatic light beam passes through a solution containing an absorbing material, the decrease in radiation intensity, along with the depth of the absorbing solution, is directly proportional to the solution's concentration and the radiation incident on it. This law is represented by this equation [46]:

$$A = \log(I_0 / I) = \boldsymbol{\varepsilon\, c\, l} \quad \text{(II- 1)}$$

Where I_0: is the intensity of incident light.

I: Intensity of light transmitted by the sample solution.

c: Represents the solute concentration.

l: Represents the length of the sample cell.

ε: Represents the molar absorption coefficient.

The ratio (I/I_o) is known as the transmittance (T) and the logarithm of the ratio

inverse (I_0/I) is known as the absorbance (A). Therefore:

$$\boldsymbol{A} = -\boldsymbol{log}\ (I / I_0) = -\boldsymbol{logT} = \boldsymbol{\varepsilon c} l \quad \text{(II-2)}$$

Where:

$$\boldsymbol{A} = -\boldsymbol{logT} \quad \text{(II-3)}$$

SO:

$$\boldsymbol{A} = \boldsymbol{(1/T)} \quad \text{(II-4)}$$

Determination of the optical band-gap as modifier (optical energy levels) (Eg):

The optical band-gap as modifier (Eg) can be estimated determined extrapolation from the absorption limit, which is provided using the Tauc relation [47]

$$(\boldsymbol{\alpha h v}) = (\boldsymbol{h v} - \boldsymbol{E g^{opt}})^{n} \quad \text{(II-5)}$$

Where α is the absorption coefficient, A is a constant, hν is the light energy and n is a constant depending on the nature of the electronic transition, Eg^{opt} is the optical band-gap as modifier energy, and the exponent n=1/2 for the direct allowed transition, while n=2 for the indirect allowed transition.

The energy gap was determined from the crossing point of the absorption edge's linear section with the energy axis.

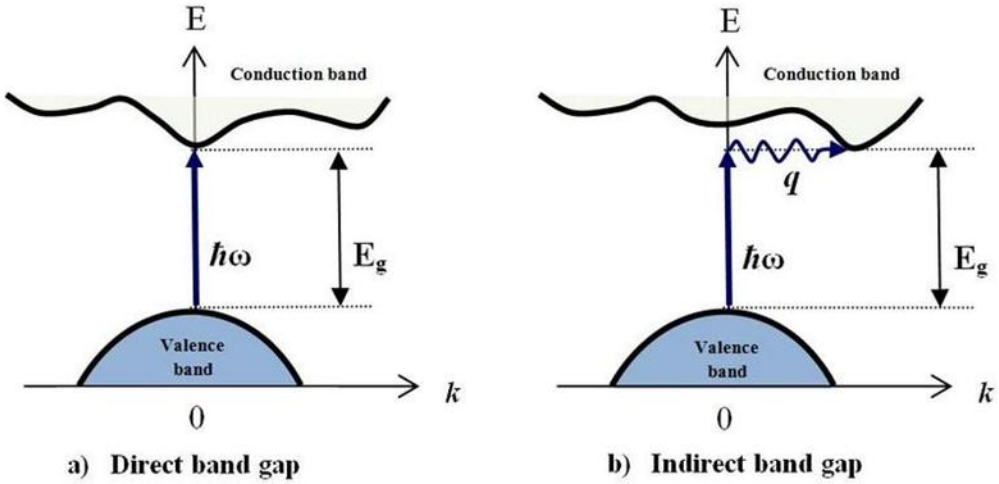

Figure (II-1): Transition electronics in the case of a semiconductor (a) to an indirect gap and (b) to a direct gap. [48]

Figure (II-2) : Ultraviolet-Visible Spectroscopy (UV-Vis)

II-3 Fourier Transform Infrared Spectroscopy (FTIR)

Infrared spectroscopy allows rapid and straightforward analysis examination of both organic and inorganic material. It is a method that can gather details regarding the various functional groups from the peak locations in the spectrum, and insights concerning the identifying and stabilizing of nanoparticles may also be deduced from this assessment. Due to the absorption of infrared energy by the examined substance, it facilitates, through the sensing of the distinctive oscillations of the chemical bonds, the analysis of the chemical groups present in the material. In these analyses, the analysis is typically performed in the middle-infrared region between 4000 and 400 cm-1 [49]. This is achieved by depositing a film of the material to be scrutinized in contact with a prism with a high refractive index and relies on the presence of an evanescent wave that travels in an area very near the crystal's exterior. Since our samples are powders, adequate contact with the ATR crystal is achieved by applying pressure [49].

II-3-1 Principle

The fundamental concept of FTIR relies on the absorption of infrared radiation in single- or double-beam mode by the substance under examination. It facilitates, through sensing the distinct vibration rates of chemical bonds, the assay of the chemical groups existing in the material. The infrared ray is guided toward the Michelson interferometer, which will vary the frequency of each wavelength of the beam differently. In this device, the incoming light beam is divided into two

parts by a beam splitter. These two portions will are reflected by mirrors, one stationary and the other movable. When the two beams merge again, destructive or constructive interference occurs based on the position of the moving mirror. The modulated beam is subsequently reflected off the two mirrors toward the specimen, where attenuations happen. The beam then reaches the detector to be converted into an electrical output [50].

II-3-2The device

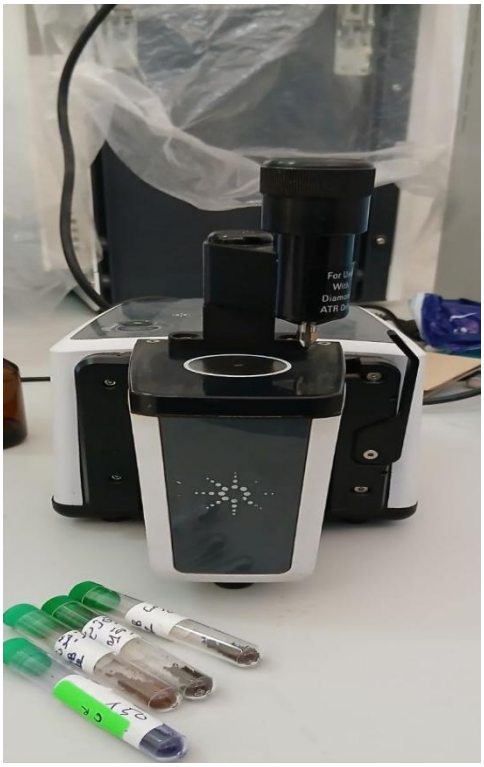

Figure (II-3): Fourier Transform Infrared Spectroscopy (FTIR)

II-4 X-ray Diffraction (XRD)

X-rays are electromagnetic waves with wavelengths spanning from 0.01 to 10 Å. This is the most frequent and broadly employed non-destructive method for determining the characteristics and structure of crystalline materials. Moreover, X-ray diffraction provides information about the crystal, like its dimensions and alignment. [51]

II-4-1 Principle

This method stems from the interaction between a sample's crystal structure and short-wavelength monochromatic radiation. The monochromatic X-ray beam is aimed at a polycrystalline substance and hits the crystal planes, where they meet the electron clouds of atoms forming that plane. In this situation, the X-ray is partly are reflected by the first plane, or they continue without interaction and can proceed to partially reflect in the subsequent plane. These planes are spaced by fixed intervals that shift according to the characteristics of the material being examined (lattice spacing). The rays' interaction might result in either reinforcing or canceling interference. Bragg's formula can be employed to ascertain the orientations where the interferences reinforce, recognized as diffraction maxima [51].

* **Bragg's law**

When a crystalline material is exposed to X-radiation of wavelength λ at an angle θ, the radiation is diffracted if Bragg's law holds true, as depicted in Figure II-4.

$$\boldsymbol{n\lambda = 2dhklsin\theta} \quad \text{(II-6)}$$

Where: n is an integer representing the order of the reflection.

λ: is the wavelength of the X-rays.

d: is the interplanar spacing.

θ: is the angle of incidence of the X-rays.

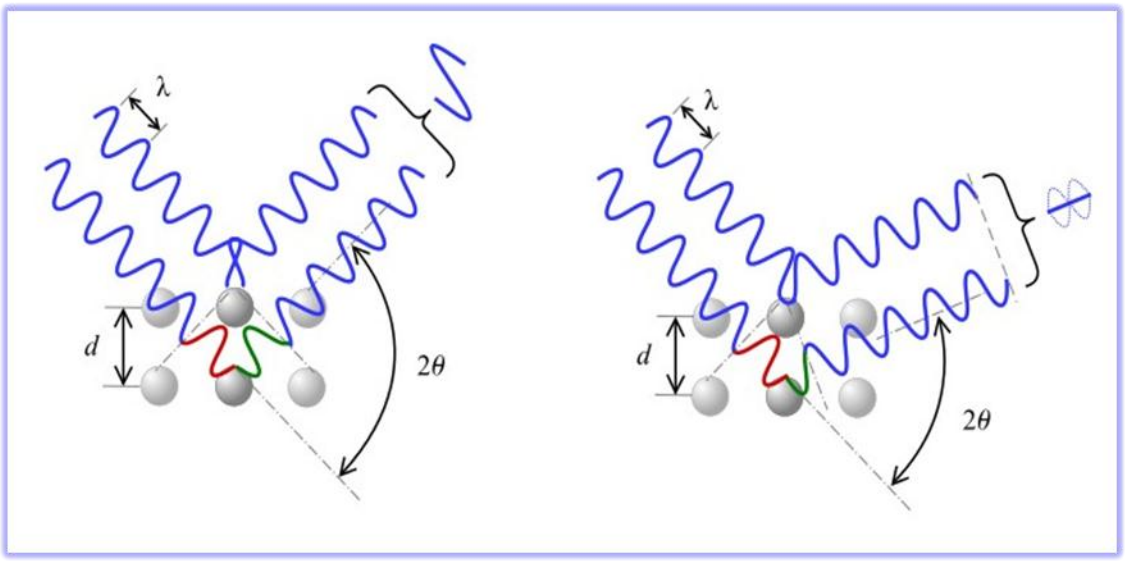

Figure (II-4): Diagram illustrating the principle of Bragg's law. [48]

Generally, the diffractogram is a chart of the diffracted intensity as a function of the angle 2θ formed with the main beam. Examination of the diffractogram allows deriving a great deal of data regarding the structural and microstructural features of the specimen, such as crystalline lattices, crystal size (D), crystallinity degree (CrI), and crystallite shape.

* **Crystallite size determination (D)**

Although various methods have been outlined for size evaluation using XRD, the Debye-Scherrer formula is the most frequently employed for crystalline dimension ascertainment [52].

$$\boldsymbol{D = k\lambda/\beta cos\theta} \text{ (II -7)}$$

Where:

D: is the crystallite size in nm .

λ : is the wavelength of the X-ray beam .

θ : is the diffraction angle.

β is the full width at half maximum expressed in radians.

In this study, X-ray diffraction (XRD) was performed using the Miniflex 600 equipped with Cu-kα radiation of wavelength = 1.5418. The diffractometer patterns were recorded at ambient temperature, and the 2θ range was scanned from 10 to 80°.

*** Crystallinity index (CrI)**

The crystallinity degree (CrI) was determined from the XRD patterns following the Segal procedure [53]:

$$\boldsymbol{CrI}\ (\%) = ((\boldsymbol{I_{002}} - \boldsymbol{I_{am}})/\boldsymbol{I_{002}}) \times \mathbf{100} \qquad \text{(II-8)}$$

Where I_{002} is the maximum (002) lattice diffraction intensity and I_{am} is the diffraction intensity.

II-4-2The device

Figure (II-5):X-ray Diffraction (XRD)

II -5 X-ray fluorescence spectroscopy (XRF)

X-ray fluorescence (XRF) analytical technique is an analytical method used to determine the chemical composition of various types of materials, which may be solid, liquid, powdered, filters, or in any other form. Sometimes, XRF technology can also be used to determine the thickness and composition of layers and coatings [54].

II-5-1 Principle

When high-energy X-rays interact with matter, they cause ionization of some atoms by ejecting some electrons. If the radiation energy is sufficient to displace an inner electron tightly bound within the atom to the nucleus, the atom becomes unstable. Then, one of the outer electrons transitions to a lower energy level to fill the place of the missing inner electron, and during this process, the excess energy over the energy of this electron in the new level close to the nucleus is released in the form of radiation.

The emitted radiation consists of electromagnetic waves with lower energy than the energy of the primary X-rays incident on the matter and is called(fluorescent radiation).

The energy of the photons of the emitted radiation has confined and distinct values, resulting from transitions between specific electron orbitals in the element [54].

II-5-2The device

Figure (II-6): X-ray Fluorescence spectroscopy [55]

II-6 Scanning Electron Microscope (SEM)

Scanning electron microscopy (SEM) is a technique used to examine of the surface morphology of solid materials and is a testing procedure that scans a specimen with an electron beam at high magnifications to produce high-resolution magnified images for examination and measure very small features. The approach is utilized quite effectively in microanalysis and failure investigation of solid inorganic substances, so this expertise presents several benefits in morphology and size analysis.

The morphology of the samples was examined utilizing a TESCAN VEGA3 scanning electron microscope (SEM). The instrument is equipped with an energy-dispersive X-ray spectroscopy (EDS) system.

II-6-1 Principle

Scanning electron microscopy is a method utilizing electron–matter interactions to observe the surface topography of solid samples. SEM furnishes images of the surface via the interaction/scattering of electrons by the material. These visuals are primarily created utilizing surface electron emissions (secondary electrons and backscattered electrons). The interaction between the beam of electrons with energy E0 (primary electrons) and the specimen yields low-energy electrons called secondary electrons. These are subsequently accelerated toward a detector whose role is to amplify the electrical signal received (at each location, intensity is converted into an electrical signal). the emitted signals are detected by different detectors, enabling the reconstruction of a three-dimensional image of the surface. Furthermore, it employs the other interactions of primary electrons with the specimen: the escape of backscattered electrons, absorption of primary electrons, along with the radiation of X photons. Each of these interactions is frequently important for the topography and the makeup of the surface, and it supplies data regarding the relationships between different surface features [56].

It is not a conventional optical microscope in the optical sense of the expression:

•There is no image creation by an objective lens (as happens in optical microscopy and in transmission electron microscopy).

• Here, the image is generated successively by sweeping the sample's surface with an electron ray and gathering the secondary electrons, that is, the backscattered ones[57].

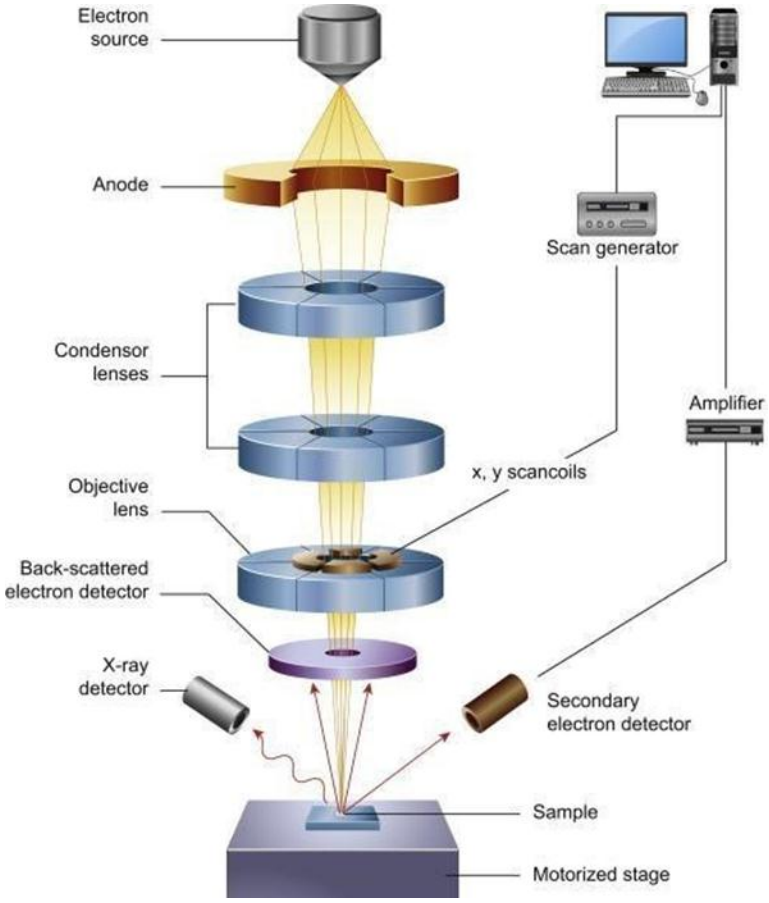

Figure (II-7): Schematic Diagram of Scanning Electron Microscope. [48]

II-6-2The device

Figure (II -8): Scanning Electron Microscope

II-7 Conclusion

At the end of this chapter, it can be said that characterization techniques are considered essential tools in the study of materials and understanding their physical and chemical properties, as they enable the determination of their internal structure and link it to their overall behavior. These techniques are also regarded as an important stage in any scientific study aimed at analyzing materials and accurately evaluating their properties.

Based on this, the next chapter will address hydrogen production through photocatalysis by reviewing its basic concepts and the most important related aspects.

CHAPTER THREE: HYDROGEN PRODUCTION BY PHOTOCATALYSIS

III-1 Introduction

Recently, the increasing demand for energy and the ecological problems resulting from abundant fossil fuel use have spurred the quest for clean and sustainable alternatives. Hydrogen has appeared as a promising energy carrier owing to its high energy density and its environmentally friendly nature, since its burning yields just water without harmful emissions [58].Among the sophisticated approaches for hydrogen production, photocatalysis has attracted considerable attention. This technique employs solar power to energize semiconductor materials, allowing the splitting of water into hydrogen and oxygen via light uptake, charge carrier creation, and subsequent redox reactions at the catalyst surface [59]. The capability of transforming solar power into storable chemical energy has attracted substantial research attention, especially following the contributions of Nathan S. Lewis and Daniel G. Nocera, who emphasized solar-fueled hydrogen generation as a vital hurdle in renewable power advancement [60]. Consequently, extensive efforts have been undertaken to enhance catalyst effectiveness and system performance.Despite these strides, several obstacles persist, encompassing low efficiency, rapid recombination of charge carriers, and restricted visible light absorption in certain substances [61]. Thus, current studies concentrate on designing more productive and stable photocatalysts [62].

In this section, this chapter covers the background of hydrogen production via photocatalysis, along with outlining the diverse techniques utilized for its production and the categories of elements used in this procedure. Furthermore, we will discuss the principal benefits and drawbacks of hydrogen, intending to offer a distinct and thorough survey of this domain and its potential in renewable energy.

III-2 History of Hydrogen Production by Photocatalysis

In 1921, Baly first discovered the concept of photocatalysis, giving it a meaning connected to all phenomena in which light radiation accelerates the reaction [63].

The term photocatalysis also refers either to catalytic reactions occurring under the influence of light or to the overall phenomena associated with photochemical activities and catalytic activities [64].

The accepted definition remains: the change in the rate of a chemical reaction or its initiation under the influence of visible or ultraviolet light in the presence of a substance (the photocatalyst)[65].

The first research was published in 1964 by Doerffler and Hauffe, in which photocatalysis was used as an indication that the combination of the catalyst and light affects the reaction [66].

In 1972, Fujishima and Honda also demonstrated the decomposition of water on the surface of a TiO2 electrode under ultraviolet light [67].

III-3 Methods Used for Hydrogen Production

III-3-1 Water Electrolysis

Water electrolysis is considered one of the most prominent sustainable methods for producing green hydrogen, as it relies on using electricity generated from renewable sources such as solar and wind energy to break down water into hydrogen and oxygen [68].

The water electrolysis technique – where water consists of a one oxygen atom bonded to two hydrogen atoms – is a common method, where the water molecule splits into hydrogen and oxygen, and oxygen is released during the reactionas shown in the following reactions [69]:

At the cathode

$$H_2O + 2e^- \rightarrow H_2 + O_2^- \text{ (III-1)}$$

At the anode

$$O_2^- \rightarrow 1/2\ O_2 + 2e^- \text{ (III-2)}$$

Overall reaction

$$H_2O \rightarrow H_2 + 1/2\ O_2 \text{ (III-3)}$$

There are three basic approaches to electrolysis, each characterized by a different operating mechanism and a different environmental impact related to the life cycle of the produced hydrogen[70].

III-3-1-1 Alkaline Electrolysis

This technique relies on using an alkaline solution (such as potassium hydroxide (KOH) or sodium hydroxide (NaOH)) to transfer ions between electrodes, and non-noble metal electrodes like nickel are used, operating at moderate temperature levels (60–90°C) [69]. As illustrated in the following diagram:

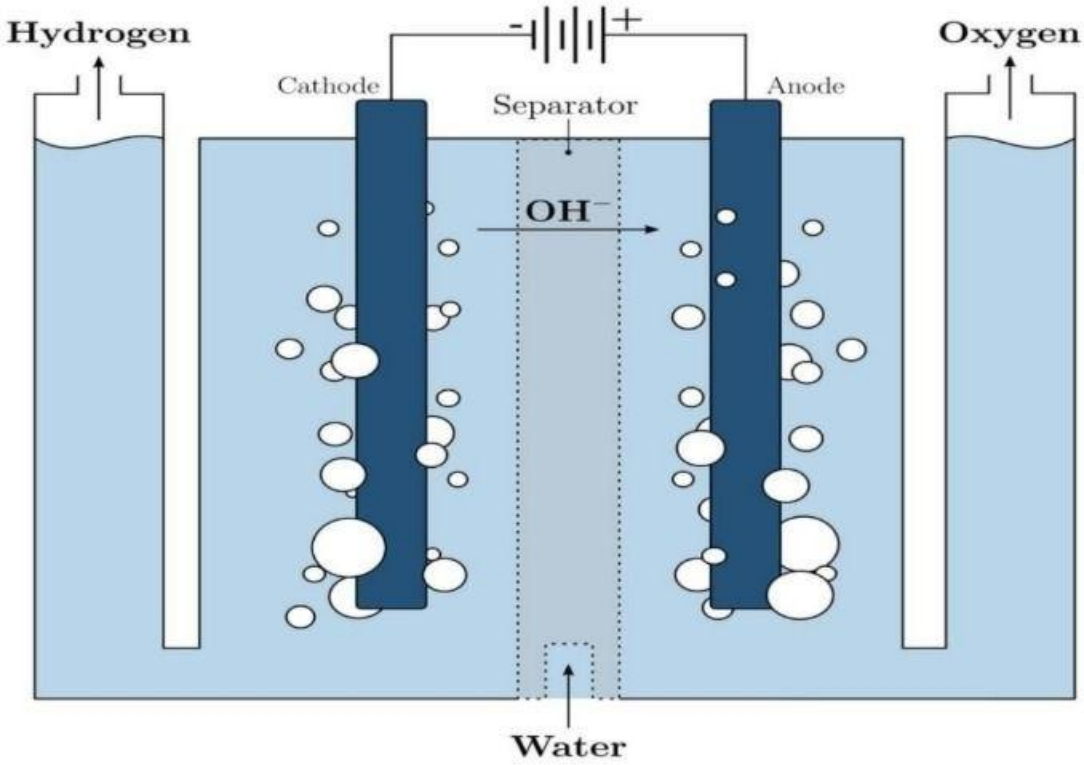

Figure (III-1): Alkaline Electrolyzer Cell [77]

Alkaline electrolysis is one of the oldest and most mature methods in the field, characterized by stability and ease of maintenance in terms of life cycle. Alkaline hydrogen is generated with low emissions provided that clean electrical energy is used, while the greatest environmental footprint occurs during equipment construction and system monitoring [70].

III-3-1-2 Proton Exchange Membrane Electrolysis

The PEM technology relies on a solid polymer membrane that allows only protons to pass through, in an acidic environment

Noble metals such as platinum and iridium are used in the electrodes, and it operates at temperatures ranging between (50–80°C) [69], as shown in the following figure:

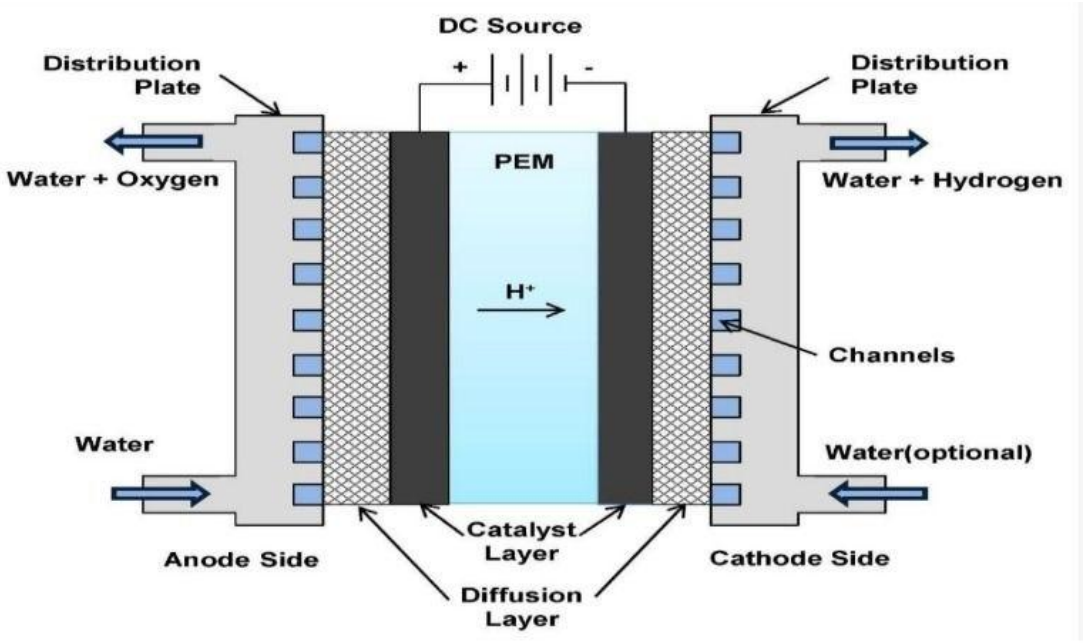

Figure (III-2): Proton Exchange Membrane Electrolysis [77]

PEM is considered one of the emerging technologies with a compact design and fast response to changes in power supply.

As for its life cycle, it produces pure hydrogen when relying on renewable energy, but the use of precious metals adds an environmental challenge during the manufacturing stages [70].

III-3-1-3 Solid Oxide Electrolysis

This method uses a ceramic electrolyte that conducts oxygen ions and operates at high temperatures reaching 900°C [71]

This cell operates as shown in the following figure:

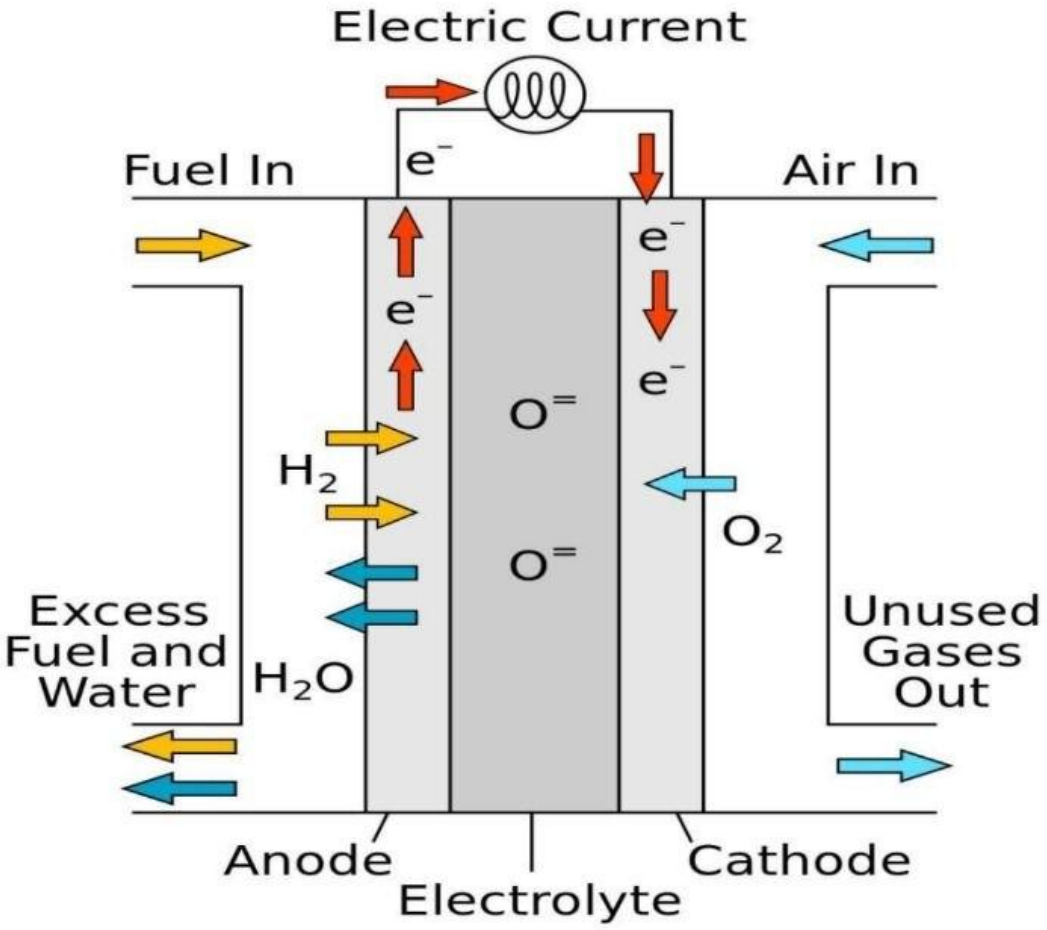

Figure (III-3): Solid oxide electrolysis [77]

SOEC is distinguished by its ability to utilize heat (whether from industrial sources or from the processes themselves), which allows saving part of the required electrical energy [68].

The life cycle of this technology is promising in terms of reducing dependence on electricity, but it is affected by the high operating temperature and the use of complex ceramic pristine materials that increase the environmental footprint during production [70].

III-3-2 Steam reforming of methane

Methane Steam Reforming is the most common industrial method for producing hydrogen, using natural gas, which mainly consists of methane CH_4 , as a main feedstock. This method is based on the reaction of methane with steam at high temperatures ranging from 700 to 1100 degrees Celsius in the presence of a metal catalyst (usually nickel Ni) to generate a mixture of hydrogen and carbon monoxide[72].

The fundamental chemical reactions in this process include:

Steam reforming reaction

$$CH_4 + H_2O \rightarrow CO + 3H_2 \quad \text{(endothermic reaction)} \quad \text{(III-4)}$$

Water-gas shift reaction

$$CO + H_2O \rightarrow CO_2 + H_2 \quad \text{(III-5)}$$

This method is widely used in the industrial sector due to its suitability and efficiency in producing large volumes of hydrogen. Although steam reforming typically produces gray hydrogen due to carbon dioxide emissions, its environmental friendliness can be improved by adopting one of the alternatives:

*Using biogas as a methane source instead of natural gas. Biogas is produced by anaerobic fermentation of organic materials such as:

_Agricultural waste (wheat straw, corn, fruit and vegetable residues)

_Animal manure (cattle and poultry waste)

_Organic household waste (food scraps)

_Sewage water

_Byproducts of food industries (dairy and slaughterhouses)

_Green waste (leaves, grass)

These materials are anaerobically fermented (in the absence of oxygen) to produce biogas, which mainly consists of methane (CH_4) and carbon dioxide (CO_2), and can be refined for use in hydrogen production via steam reforming or in electricity generation.

Integrating technology with Carbon Capture, Utilization, and Storage (CCUS) systems reduces CO_2 emissions generated and converts hydrogen into "blue" hydrogen [73], which may be considered "green" under certain conditions if it relies on renewable energy sources to operate the system .

III-3-3 Solar Thermochemical Hydrogen Production

The solar thermochemical method for hydrogen production is considered one of the most promising future methods for producing emission-free green hydrogen. This method relies on exploiting Concentrated Solar Power (CSP) to generate high temperatures exceeding 1000°C to drive thermochemical reactions that decompose water (H_2O) into its primary elements: hydrogen (H_2) and oxygen (O_2)[74].

In this method, mirrors or lenses are used to concentrate sunlight onto a thermal reactor containing intermediate materials, such as metal oxides (cerium oxide or zinc oxide), which undergo a two-step thermal process:

*First stage (reduction): The metal is heated by concentrated solar energy until it partially decomposes and releases oxygen at (T > 1500°C)

$$ZnO \rightarrow Zn + \tfrac{1}{2}O_2 \quad \text{(III-6)}$$

*Second stage (oxidation): The reduced metal reacts again with water vapor to produce hydrogen:

$$Zn + H_2O \rightarrow ZnO + H_2 \quad \text{(III-7)}$$

The metal oxide material is reused in continuous cycles, making the process theoretically efficient

No carbon emissions are generated during operation, making the resulting hydrogen completely pure.

It relies on a renewable and free energy source (the sun), making it viable for long-term application. High thermal efficiency is anticipated despite current technical challenges, but recent research demonstrates the possibility of developing solar reactors with high conversion rates.

Among the technical difficulties it faces is that it requires technology that demands very high temperatures exceeding 1000°C, necessitating modern solar concentration systems. Additionally, sunlight availability is limited to daylight hours, and the intermediate materials face challenges related to withstanding repeated thermal cycles [74].

III-3-4 **Biophotolysis**

Biophotolysis is considered one of the most promising methods for producing green hydrogen using solar energy and microorganisms such as green algae and cyanobacteria. This approach is characterized by its ability to directly convert solar energy into chemical energy in the form of hydrogen gas, through microbiological pathways involving enzymes like hydrogenase and nitrogenase [75].

This technology is classified into two main types:

*Direct biophotolysis, where algae or cyanobacteria split water under sunlight into hydrogen and oxygen with the help of the hydrogenase enzyme[75].

*Indirect biophotolysis, which occurs when organisms store starches during photosynthesis and later utilize them to produce hydrogen under anaerobic conditions[75].

Although this technology is environmentally friendly and does not require massive external energy inputs, one of the main challenges it faces is enzyme instability, low conversion efficiency, and its current lack of readiness for large-scale industrial application.

III-3-5 Photocatalysis

It is a modern technique for hydrogen production using light (mostly from the sun) and semiconductor photocatalysts that split water into hydrogen and oxygen without carbon emissions [76]. Among the most prominent of these catalysts are TiO_2 , MnO_2 , and $Al_2\ O_3$, and some of these elements have demonstrated outstanding performance in experimental tests.

The mechanism begins when the catalyst absorbs photons, generating electrons and holes that move to the surface of the material and participate in water reduction reactions as follows:

$$H^+ + 2e^- \rightarrow H \quad \text{(III-8)}$$

$$H_2\ O + 2H^+ \rightarrow \tfrac{1}{2}O_2 + 2H \text{ (oxidized)} \quad \text{(III-9)}$$

Experiments conducted at the University of Ouargla showed that MnO_2 acts as an effective photocatalyst in an alkaline medium (13.59%), while TiO_2 and $Al_2\ O_3$ acted as inhibitors at rates of -4.29% and -24.68% respectively at a concentration of 10 g/l. The combination of 75%

TiO_2 with 25% MnO_2 contributed to an increase in yield by 23.06%, with the best efficiency observed when using 30 g/l of KOH as the electrolyte solution, which raised the yield by 26%.

On the other hand, there are emerging research trends toward developing organic catalysts based on carbon, which are environmentally friendly and free of heavy metals. One model is the creation of organic polymers used as effective catalysts under visible light [77].

III- 4 Types of materials used

Types of photocatalysts: To achieve the goal of photocatalysis, a wide range of homogeneous and heterogeneous photocatalysts have been produced. The heterogeneous photocatalyst is often in a solid state, and the reacting materials are in a liquid form, so the chemical reaction occurs on the surface of the catalyst, which requires the adsorption of the reactants on its surface first. In homogeneous catalysis, the consistency of the reactants and the catalyst is in the same state (usually liquid state)[78]. We mention some examples of homogeneous and heterogeneous photocatalysts as follows[78]:

Heterogeneous catalysts:

CuO; ZnS; SnO_2; SnS_2; ZnO; TiO_2

Homogeneous catalysts:

CuO; $BiVO_4$; g-C_3N_4; $BiPO_4$; WO_3

III-5 Advantages and Disadvantages

III-5-1 Features

III-5-1-1 Sustainable

Green hydrogen does not emit harmful gases either during combustion or manufacturing.

III-5-1-2 Storage capability

Hydrogen is easy to store, allowing it to be used later for different purposes and at times other than immediately after its production.

III-5-1-3 Versatility

Green hydrogen can be converted into electrical energy or synthetic gas and used for household, commercial, industrial, or transportation purposes[79].

III-5-2 Disadvantages

III-5-2-1 High-energy consumption

The production of hydrogen in general and green hydrogen in particular, requires more energy than other fuel sources.

III-5-2-2 Safety concerns

Hydrogen is a highly unstable element and prone to ignition, so comprehensive safety measures must be implemented to avoid leaks and explosions [79].

III-6 Conclusion

Based on what has been presented in this chapter, it is clear that hydrogen generation through photocatalysis represents a promising technology that combines sustainability and energy efficiency, despite the challenges related to yield and the stability of the components. The examination of various methods and materials used has shown that enhancing the performance of catalysts remains the pivotal element for the development of this technology. Therefore, progress in this field is fundamentally linked to the search for more effective raw materials that enable the achievement of a comprehensive practical application of green hydrogen.

PRACTICAL PART

CHAPTER ONE: MATERIALS AND METHODS

I-1 Materials and Equipment

I-1-1 Materials

Germanium(IV) ethoxide, Titanium(IV) isopropoxide, Aluminum Perchlorate, Urea solution, Ultrapure Water, Nitrogen Gas, 2-Propanol, Methanol, Ethanol, Triethanolamine, Benzoquinone, Isopropanol, Ethylenediaminetetraacetic Acid, Silver Nitrate, $Na_2\ SO_4$,

I-1-2 Equipment

PTFE containers, Autoclaves, Dialysis, closed quartz reactor, magnetic stirrer, xenon lamp, gas chromatograph, thermal conductivity detector (TCD), solar simulator, molecular sieve 5 Å column, UV–Vis spectrophotometer, X-ray diffractometer, FTIR , X-ray fluorescence spectrometer, scanning electron microscope, rectangular quartz cell,

I-2 Synthesis of Ti-Imogolite

The Ti/Ge sample was prepared with a molar ratio defined as x = [Ti]/([Ge] + [Ti]) = 0.2. Germanium(IV)ethoxide and titanium(IV) isopropoxide were used as metal alkoxide precursors and were combined so that titanium accounted for 20% of the total metal alkoxide amount, whereas germanium comprised the remaining 80%. The precursors were mixed under constant stirring in the presence of an aluminum perchlorate solution, keeping an [Al]/([Ge] + [Ti]) molar ratio of 2. The aluminum perchlorate concentration was set at 0.2 mol•L^{-1}, a state previously documented to promote high nanotube yields without causing structural alterations.

An aqueous urea solution (0.2 mol•L^{-1}) was then added as a gradual hydroxide ion source produced via thermal decomposition. The resulting mixture was stirred at ambient temperature for 1 h in PTFE containers, then moved into sealed autoclaves (Parr Instrument) for hydrothermal processing at 140 °C for 5 days under autogenous pressure.

After cooling to ambient temperature, the slurries were purified by dialysis employing 10 kDa Spectra/Por membranes against ultrapure water to eliminate excess salts and residual alcohols. Dialysis proceeded until the conductivity of the external water dropped beneath 5 μS•cm^{-1}.

I-3 Characterization Techniques

A comprehensive set of analytical techniques was utilized to study the structural, optical, chemical, and morphological properties of the prepared materials.

The optical properties of the samples were investigated via UV–Vis spectroscopy, where absorption spectra were recorded across an appropriate wavelength range. The appropriate wavelength range were calculated employing the Tauc approach by optical band gap energies versus photon energy.

The crystalline structure and phase composition were assessed using X-ray diffraction (XRD) with Cu Kα radiation ((λ= 1.5406 Å). Diffraction patterns were gathered across a set range of 2 to evaluate structural features and crystal arrangement.

The chemical bonds and functional groups present in the substances were explored employing Fourier-transform infrared (FTIR) analysis. Spectra were obtained within the middle-infrared spectrum to identify key vibrational modes linked to the framework and surface features.

The elemental makeup and elemental distribution were gauged via X-ray emission (XRF) analysis, allowing for the detection and identification of constituent elements via their unique emission signals.

The surface morphology and microstructure details were examined using scanning electron microscopy (SEM). Images were acquired at varied magnifications to inspect the surface aspect, aggregation patterns, and overall morphological features.

Furthermore, the photoelectrochemical performance of the prepared substances was assessed utilizing a three-electrode electrochemical setup, comprising a working electrode built from the synthesized matter, an opposing electrode, and a reference electrode. Assessments like linear sweep voltammetry and transient photocurrent response were performed under regulated lighting parameters.

I-4 Hydrogen Generation and Optimization Procedure

Photocatalytic hydrogen evolution experiments were carried out in a closed quartz reactor according to an established protocol [80], involving systematic optimization of the operating

parameters. Before illumination, the reaction mixture was purged with nitrogen gas for 30 min to remove dissolved oxygen. In a typical experiment, 5 mg of the photocatalyst was dispersed under continuous stirring in 20 mL of a deoxygenated aqueous solution containing a sacrificial agent.

An exhaustive optimization study was performed to assess the impact of the experimental variables on hydrogen production. The type of sacrificial agent was explored by comparing methanol (MeOH), ethanol (EtOH), and triethanolamine (TEOA), whilst the concentration of the sacrificial agent was also altered (5%, 10%, and 20% v/v). The influence of illumination settings was examined by conducting trials under UV illumination and simulated sunlight. Furthermore, the lamp–reactor distance was modified (5, 10, and 15 cm) to investigate the effect of light intensity, and diverse stirring speeds (300, 600, and 900 rpm) were employed to determine the role of mass transfer and photocatalyst distribution. Comparative experiments were additionally conducted utilizing pristine Imogolite and Ti-modified Imogolite in order to evaluate the effect of titanium inclusion on photocatalytic performance. Throughout the enhancement progression, only one factor was varied at a time whilst all other experimental conditions were kept constant.

UV–Vis irradiation was supplied by a xenon lamp (Oriel, 300 W). The amount of hydrogen evolved during the photocatalytic process was measured using a gas chromatograph (Agilent Technologies 7820A) equipped with a thermal conductivity detector (TCD) operating at 250 °C. Nitrogen was utilized as the carrier gas at a flow rate of 22.5 $mL \cdot min^{-1}$, and hydrogen was separated using a molecular sieve 5 Å column with the oven temperature held at 50 °C.

To evaluate the structural and morphological stability of the photocatalysts under reaction circumstances, selected samples were collected post-hydrogen generation trials, dried, and then examined by XRD.

I-5 Radical Scavenger Test

Scavenger tests were conducted under the optimized hydrogen production conditions identify the main active species engaged in the photocatalytic process. Before illumination, the mixture was purged with nitrogen gas for half an hour to clear out dissolved oxygen. In a typical experiment, 5 mg of the photocatalyst was suspended in 20 mL of a deoxygenated aqueous

solution containing 10% (v/v) triethanolamine (TEOA) as a sacrificial agent. The suspension was magnetically stirred to guarantee uniform dispersion of the photocatalyst.

Specific scavengers were separately introduced to the reaction mixture to capture defined reactive species, while all other experimental conditions were kept constant. Benzoquinone (BQ) was utilized as a quencher for superoxide radicals ($\bullet O_2^-$), isopropanol (IPA) served to trap hydroxyl radicals (•OH), ethylenediaminetetraacetic acid (EDTA) was introduced as a hole (h^+) quencher, and silver nitrate ($AgNO_3$) functioned as an electron (e^-) quencher. The concentration of each scavenger was selected to be ample for efficiently capturing the target species without substantially modifying the reaction environment.

Photocatalytic hydrogen evolution was achieved under UV light utilizing a xenon lamp (300 W), maintaining a lamp–reactor separation of 5 cm and an agitation rate of 900 rpm. The volume of hydrogen generated during the process was measured using gas chromatography fitted with a thermal conductivity detector, adhering to the identical analytical method detailed for the hydrogen generation tests without scavengers.

For every scavenger assessment, the hydrogen release speed was contrasted with that achieved without any scavenger present (control trial).[81]

I-6 Recycling Performance

Recycling tests were carried out under the optimized hydrogen production conditions for five consecutive cycles, indicating good stability of the photocatalysts amidst the enforced operational circumstances.

I-7 Photoelectrochemical Studies

Photoelectrochemical tests were performed using a three-electrode setup in a rectangular quartz container rectangular quartz cell, with the prepared FTO electrode (1 cm^2) as the working electrode, a platinum wire as the counter electrode, and an Ag/AgCl electrode as the reference electrode. The electrolyte comprised an aqueous 0.5 M Na_2SO_4 solution without pH adjustment. The working electrode was prepared by dispersing 10 mg of the synthesized Ti-Imogolite in 5 mL of 2-propanol, then drop-casting the suspension onto a 1 cm^2 FTO substrate. The coated electrodes weredried in air overnight at ambient temperature before testing. Linear

sweep voltammetry (LSV) was performed at a constant scan rate under illumination to evaluate the photoelectrochemical performance of the electrodes. Chopped-light chronoamperometry assessments were carried out by cyclically turning the light on and off at 20 s periods to evaluate the photoresponse stability and the current reproducibility. Illumination was supplied by a xenon lamp fitted with an AM 1.5 solar simulator. [82]

CHAPTER TWO:

RESULTS AND DISCUSSION

II-1 Characterization

II-1-1 UV–Vis Analysis

The UV-visible spectroscopic analysis of the Imogolite and Ti-Imogolite samples provides important information regarding their optical properties. The absorption spectrum in Figure 1a displays a main peak for the pristine Imogolite at 204 nm. After titanium modification, the absorption maximum of Ti-Imogolite shows a clear shift toward a longer wavelength at 249 nm. This displacement implies that the incorporation of titanium has effectively altered the electronic structure of the nanotubes, enabling them to absorb lower-energy light. The higher intensity in the UV region for the Ti-Imogolite specimen likewise points to a enhanced photoactivity relative to the pristine material.

To determine the band gap energy (Eg) of the specimens, a plot of $(\alpha h\nu)^2$ versus photon energy (eV) was constructed using the Tauc method [83]. Figure 1b, For the pristine Imogolite, the estimated band gap was roughly 3.25 eV , which is standard for wide-band-gap materials that mainly react to intense UV radiation [84]. Figure 1c, For the Ti-Imogolite, the band gap notably decreased to approximately 2.24 eV. This considerable decrease in the band gap a reduction of 1.01 eV verifies that the incorporation of Titanium introduces new electronic levels within the band gap, promoting simpler electronic transitions. This lower Eg magnitude is a strong signal that the Ti-Imogolite

nanotubescan facilitate electron transfer more effectively when subjected to light, as this shifts the absorption edge closer to the visible light spectrum. This finding aligns with the observed UV absorption shift and emphasizes the successful adjustment of the material's electronic characteristics via Titanium alteration.

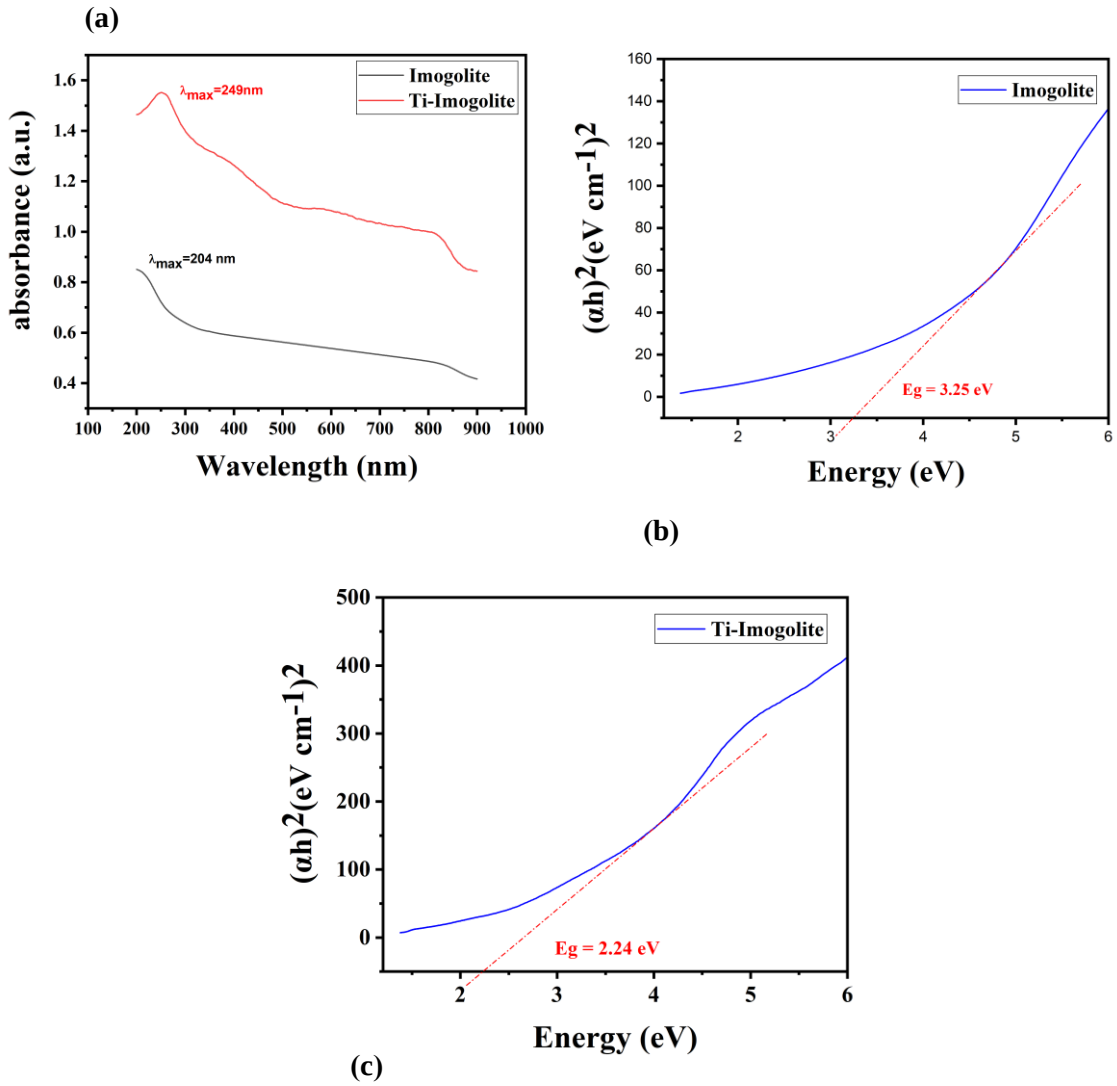

Figure 1: (a) UV–Vis absorption spectra of Imogolite and Ti-Imogolite, (b) Tauc plot for band-gap as modifier energy evaluation of Imogolite, (c) Tauc plot for band gap energy evaluation of Ti-Imogolite.

II-1-2 XRD Analysis

Figure 2 displays the X-ray diffraction patterns of pristine Imogolite and Ti-Imogolite. The pristine specimen's diffraction pattern shows three main broad reflections at approximately 2θ = 14°, 22–23°, and 34–35°. These are characteristic of Imogolite nanotubes. The reflections are generally attributed to the atomic arrangement within the curved nanotube walls of the nanotubes. The broad peak observed at a low angle demonstrates the repeating pattern of the tube wall organization, while the peak near 22–23° relates to the arrangement and packing of adjacent nanotubes into aggregates. The weaker band appearing at higher diffraction angles is linked to higher-order structural correlations within the nanotube lattice. The broad character of these reflections supports the restricted long-range crystallinity and the dominance of short-range order, which is a known structural characteristic of Imogolite substances [85, 86]

The interplanar spacing was determined using Bragg's law:[87]

$$n\lambda = 2d\sin\theta$$

where λ =1.5406 Å corresponds to Cu Kα radiation.

The calculated interplanar spacingfor original Imogolite is around 0.63nm , which is in good agreement with the typical periodic distance associated with the curved aluminosilicate nanotube structure reported for Imogolite frameworks [85, 86]

For the Ti-Imogolite sample, the determined spacing slightly decreases to 0.61 nm, indicating that the introduction of Ti species cause a slight compression within the local structural arrangement of the nanotube walls.

Despite this slight alteration, the overall diffraction pattern of the modified sample remains similar to that of the original material, indicating that the Imogolite nanotubular architecture is retained following titanium incorporation. Furthermore, the absence of additional diffraction peaks corresponding to crystalline titanium oxide phases suggests that titanium is not present as a distinct TiO_2 phase but is integrated into the Imogolite structure or highly dispersed throughout the nanotube lattice [88, 89].

These results indicate that Ti integration induces only minor structural changes while preserving the inherent nanotubular design of Imogolite, which is vital for maintaining its structural stability and functional capabilities.

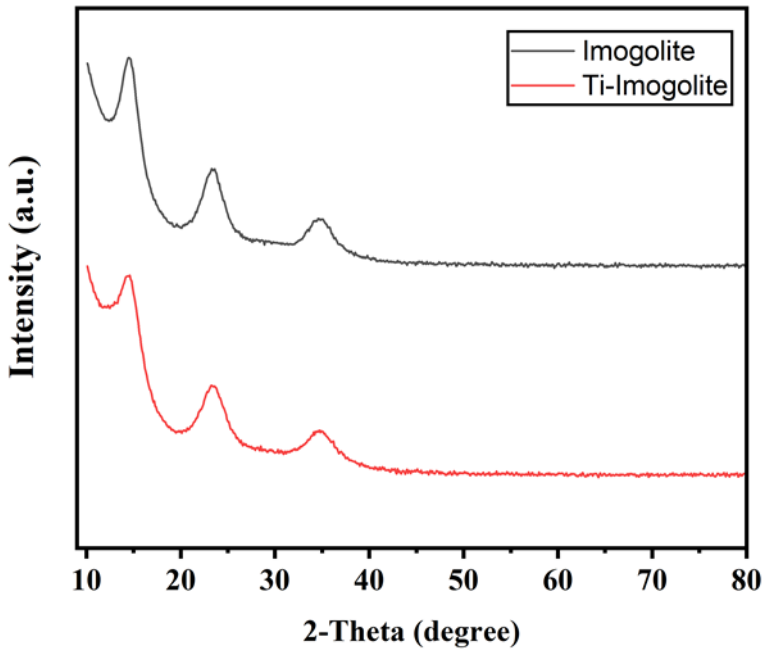

Figure 2: XRD patterns of Imogolite and Ti-Imogolite

II-1-3 Fourier Transform Infrared Spectroscopy (FTIR)

The molecular structure and functional groups of the prepared nanomaterials were examined using FTIR spectroscopy, as shown in Figure 3 FTIR spectra of pristine Imogolite and Ti-altered Imogolite. For the pristine Imogolite, the spectrum reveals a wide absorption peak at 3453 cm^{-1}, corresponding to the stretching vibrations of outer hydroxyl (O-H) groups [90]. The peak at 1644 cm^{-1} is credited to the bending vibration of adsorbed water molecules [91], while the strong band at 998 cm^{-1} denotes the characteristic Si–O–Al stretching vibrations of the aluminosilicate nanotubular framework .[92]

After modification, the Ti-Imogolite spectrum retains the basic framework of the Imogolite, verifying that the tubular shape was preserved. Nevertheless, a marked shift in the hydroxyl band to 3423 cm^{-1} indicates the reaction between titanium atoms and the surface active groups. Importantly, the appearance of a new band around 574 cm^{-1} is ascribed to the Ti-O or Ti-O-Si

vibrations [93], providing evidence of the effective incorporation of Titanium into the Imogolite composition. These findings affirm the successful preparation of the Ti-modified Imogolite composite while maintaining its structural integrity.

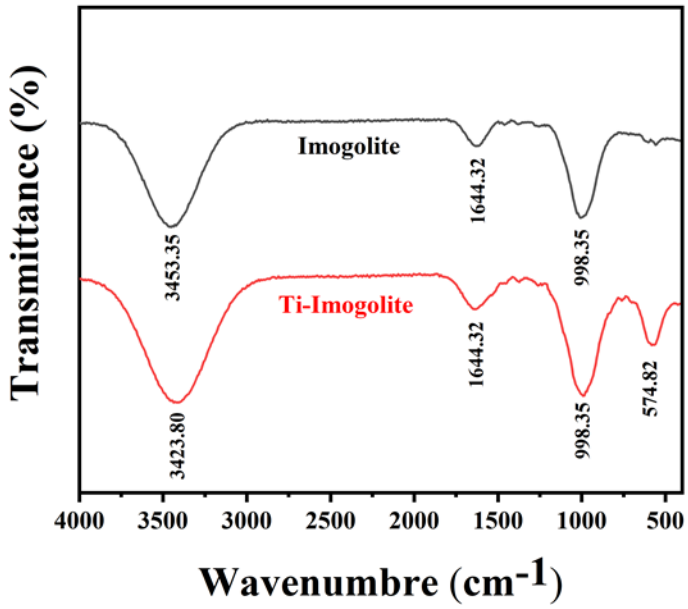

Figure 3: FTIR spectra of pristine Imogolite

II-1-4 XRF Analysis

The elemental composition of the nanotubes was investigated utilizing X-ray Fluorescence (XRF) spectrometry to confirm the effectiveness of the modification process. Figure 4 presents the XRF spectra for both (a) pristine Imogolite and (b) Ti-Imogolite. The figure shows the distinct Kα and Kβ emission lines for every element detected in the samples.

In Figure 4a, the spectrum of the pristine Imogolite is characterized by an extremely intense and narrow peak at 1.49 keV. This spectral line corresponds to Aluminum (Al) and confirms that the nanotubes consist of aluminosilicate material. It should be noted that the Silicon (Si) peak, generally observed at 1.74 keV, is not apparent as an independent peak. This occurs since it is quite near the dominant Aluminum peak, leading them to merge and appear as a single

unresolved peak. This is a typical occurrence in XRF when examining light elements possessing adjacent energy levels.

In Figure 4b, the successful incorporation of titanium into the Imogolite framework is clearly indicated by the emergence of two novel and distinct peaks. The primary emission at 4.49 keV is attributed to Titanium (Ti Kα), whereas the weaker peak at 4.92 keV corresponds to Titanium (Ti Kβ). These energy values align with the established reported values for Titanium (4.51 keV and 4.93 keV) closely. The slight difference (≈ 0.02keV) could stem from the new chemical linkages formed between Titanium and the Imogolite matrix (Ti-O-Al/Si).

Furthermore, both spectra exhibit some additional peaks at greater energy magnitudes. The emissions at 9.86 keV and 10.95 keV are recognized as Zinc (Zn) spectral lines (Kα and Kβ) . These are probably minor contaminants originating from the apparatus components or the specimen support and they do not impact the integrity of the Imogolite. Moreover, a weak peak at 1.18 keV indicates a trace quantity of Magnesium (Mg) from the precursors employed during the preparation. Lastly, given that the Aluminum signals remain robust in the Ti-Imogolite sample, this suggeststhat the tube architecture was preserved and was not degraded following the introduction of titanium.

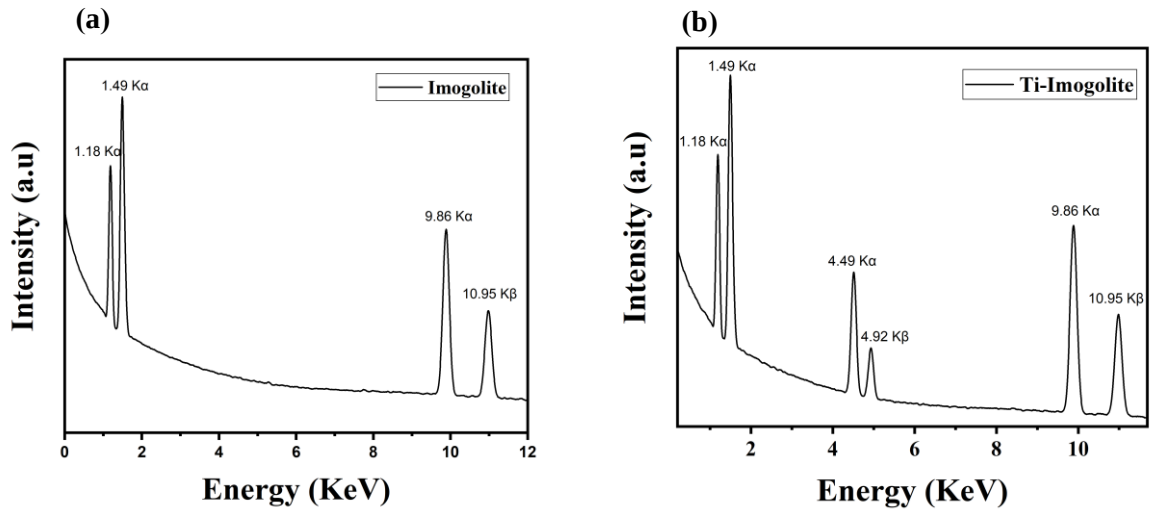

Figure 4: XRF spectra of (a) Imogolite and (b) Ti-Imogolite showing Kα and Kβ emission lines

II-1-5 SEM Morphological Analysis

The surface morphology of the prepared samples were investigated using scanning electron microscopy, and the corresponding SEM images are displayed in Figure 5(a–b).

As seen in Figure 5(a), the pristine Imogolite sample displays irregular aggregates composed ofdensely packed fibrous and fiber-like nanostructures. These formations result in compact aggregates with uneven surfaces and poorly defined boundaries. At greater magnification, the sample appears as an intertwined web of short cylindrical or rod-like units that are randomly oriented and strongly entangled. This form is typical of Imogolite nanotubes, which tend to cluster into bunches and aggregates throughout the hydrothermal creation owing to powerful molecular attractions. The existence of gaps and spaces between the groupings also suggests a porous composition.

In contrast, significant morphological changes are detected following titanium inclusion. As depicted in Figure 5(b), the Ti-Imogolite specimen still retains a clustered appearance; nevertheless, the aggregates appear denser and more distinct compared to the initial substance. The micrograph reveals the presence of larger and longer rod-like structures integrated within granular agglomerates. These elongated units are more clearly observed than the fibrous structures seen in the initial specimen. Furthermore, the surface of these aggregates seems coarser and more uneven, pointing to the presence of small nanoscale features decorating the structure.

A direct comparison between Figure 5(a) and Figure 5(b) plainly illustrates that titanium addition alters the appearance of the Imogolite groupings. Whereas the pristine sample is mostly characterized by loosely packed fibrous clusters, the Ti-modified sample shows thicker rod-like bundles and tighter groupings. Despite these structural alterations, the general nanotubular framework of Imogolite stays intact, implying that the titanium presence mainly impacts the clumping and external texture rather than damaging the original tube structure. These morphological changes suggest that the inclusion of titanium influences the initiation and growth process during synthesis, resulting in the creation of more compact nanotube bundles and a coarser exterior appearance.

(a) (b)

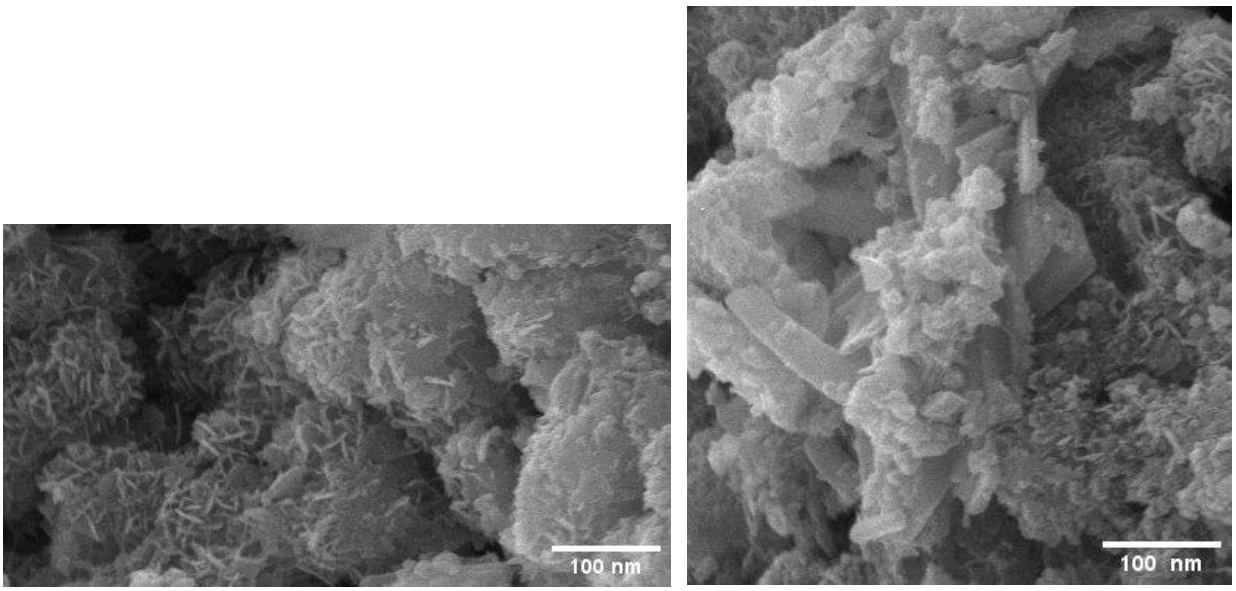

Figure 5: SEM images of (a) pristine Imogolite and (b) Ti/Ge-Imogolite

II-2 Photoelectrochemical Characterization

The photoelectrochemical (PEC) propertiesof pristine Imogolite and Ti-Imogolite were evaluated to understand the efficacy of charge-carrier generation and transport under illumination. Figure 6a displays the linear sweep voltammetry LSV curves recorded in both dark and illuminated conditions utilizing a 0.5 M Na2SO4 solution.

Without illumination (Dark), both electrodes show a low current density, verifying the electrochemical stability of the nanotubes and the lack of any undesired side reactions. Nevertheless, under illumination, a notable photo-response is noticed. The Ti-Imogolite contact achieves a maximum photocurrent density of roughly 14 mA cm-2 at 1.2 V, which is more than three times higher than that of raw Imogolite (4 mA cm-2). Moreover, Ti-Imogolite displays a lower onset potential (near 0.6 V), suggesting that incorporating titanium lowers the energy threshold and facilitates the separation of the photo-generated electrons and holes.

To evaluate the stability and reproducibility of the photo-response over time, chopped-light chronoamperometry (i-t) measurements were conducted at 20 s intervals, as depicted in Figure 6b. Each time the light is switched on, both specimens present a swift rise in photocurrent, which rapidly returns to the baseline when the light is switched off. Ti-Imogolite exhibits a considerably

greater and steadier photocurrent (ranging from 0.35 to 0.45 mu A) in contrast to the very weak response of the unmodified material.

The steady and ordered pattern of these photocurrent responses in Figure 6b confirms that the Ti-Imogolite structure is robust and preserves its capability during continuous operation. This enhanced output stems from the titanium adjustment, which generates novel electronic levels that aid in absorbing more light and prevent the charge carriers from quickly reuniting. These findings directly demonstrate that Ti-adjustment is a very fruitful method for enhancing light-harvesting performance of these tubes for sun-powered uses.

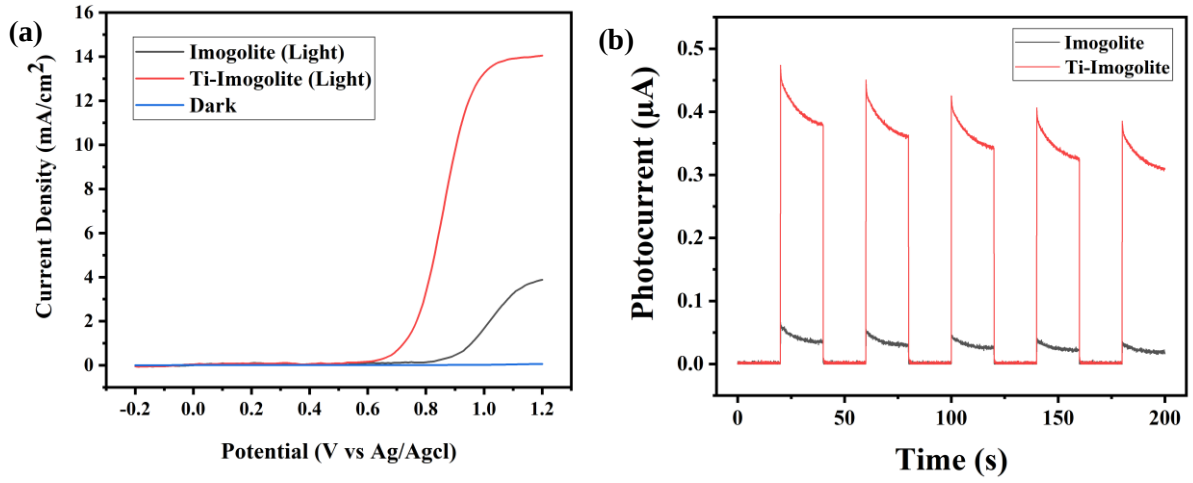

Figure 6: (a) Linear sweep voltammetry (LSV) curves under light and dark conditions, and (b) transient photocurrent response (I–t curves) under chopped light illumination for pristine Imogolite and Ti-Imogolite.

II-3 The Photocatalytic Hydrogen Production

II-3-1 Optimization

The photocatalytic hydrogen evolution results summarized in Table 1 demonstrate a notable dependence of the hydrogen evolution rate on both the operational parameters and the photocatalyst composition. When methanol was used as the sacrificial agent under UV illumination with a lamp–reactor distance of 10 cm and a stirring speed of 600 rpm, hydrogen evolution rates of 57 and 388 µmol g^{-1} h^{-1} were observed for Imogolite and Ti-Imogolite,

respectively. This outcome is consistent with established mechanisms where hydrogen formation is ascribed to light-mediated sacrificial-agent oxidation .[81]

while employing ethanol under identical settings yielded even lower values of 42 and 364µmol g^{-1} h^{-1}. Conversely, replacing alcohols with triethanolamine (TEOA) resulted in a considerable increase in hydrogen evolution, providing 73 µmol g^{-1} h^{-1} for Imogolite and 415 µmol g^{-1} h^{-1} for Ti-Imogolite at 10% TEOA. This pronounced improvement quantitatively illustrates the superior hole-scavenging ability of TEOA, which suppresses charge recombination more effectively than alcohol-derived donors. The effect of TEOA concentration further emphasizes this trend, as decreasing the concentration to 5% decreased the hydrogen evolution rate to 61 µmol g^{-1} h^{-1} for Imogolite and 403 µmol g^{-1} h^{-1} for Ti-Imogolite, whereas increasing it to 20% yielded slightly reduced figures of 68 and 398 µmol g^{-1} h^{-1}, respectively. These data suggest that 10% TEOA represents an optimal equilibrium between effective hole scavenging and favorable optical and mass-transfer conditions. The impact of the light source is evident when comparing UV illumination with simulated solar light, where hydrogen evolution decreased from 73 to 46 µmol g^{-1} h^{-1} for Imogolite and from 415 to 377 µmol g^{-1} h^{-1} for Ti-Imogolite, reflecting the diminished photon energy and absorption proficiency under solar simulation. Photon-flux effects are further substantiated by altering the lamp–reactor spacing, as decreasing the separation from 15 to 5 cm increased hydrogen evolution from 64 to 85 µmol g^{-1} h^{-1} for Imogolite and from 409 to 442µmol g^{-1} h^{-1} for Ti-Imogolite, due to the greater quantity of incident photons reaching the catalyst surface. Mass-transfer effects were plainly noticed upon increasing the stirring velocity from 300 to 900 rpm at a set distance of 5 cm, where hydrogen evolution rose from 71 to 96 µmol g^{-1} h^{-1} for Imogolite and from 431 to 470 µmol g^{-1} h^{-1} for Ti-Imogolite, verifying that improved spreading and diffusion substantially enhance photocatalytic performance. Under the concurrent optimized conditions—TEOA at 10%, UV illumination, a lamp–reactor separation of 5 cm, and a stirring speed of 900 rpm—the highest hydrogen evolution rates of 96 µmol g^{-1} h^{-1} for Imogolite and 470 µmol g^{-1} h^{-1} for Ti-Imogolite were attained. Across all trial settings, Ti-Imogolite consistently outperformed pristine Imogolite, with activity enhancements ranging from roughly sixfold under methanol to almost fivefold under ideal settings, highlighting the important role of titanium inclusion. This improvement stems from the modification of the electronic structure induced by Ti species, which introduce electron-accepting sites that aid charge segregation and

reduce recombination, supporting theoretical predictions on the internal wall polarization of these 1D nanotubes [94, 95]

The photocatalytic reaction employing triethanolamine (TEOA) as a sacrificial electron provider is known to significantly enhance hydrogen evolution due to its strong hole-scavenging ability and favorable oxidation kinetics. The hydrogen generation pathway is anticipated to adhere to a process similar to that documented for TiO_2 based assemblies in the presence of amine-type sacrificial agents, with main differences stemming from TEOA's multidentate form. Upon light irradiation, the Ti-Imogolite based photocatalyst undergoes photoexcitation, creating electron–hole pairs as per: [84]

$$\text{Ti-Imogolite} + h\nu \rightarrow e^- \text{ CB} + h^+ \text{ VB} \quad (1)$$

The photogenerated holes are rapidly scavenged by TEOA molecules adsorbed onto the photocatalyst exterior. Because of the presence of tertiary amine and hydroxyl groups, TEOA can effectively transfer electrons and undergo sequential oxidative breakdown. The initial hole oxidation of TEOA results in the creation of a radical cation and the release of protons: [96]

$$\text{TEOA} + h^+ \text{ VB} \rightarrow \text{TEOA}^{\bullet +} + H^+ \quad (2)$$

The TEOA radical cation is unstable and undergoes further dealkylation and C–N bond scission processes, forming intermediate species like diethanolamine, aldehydes, and iminium-type compounds, while continuously providing protons to the reaction medium: [97]

$$\text{TEOA}^{\bullet +} + H_2\text{O} \rightarrow \text{oxidized intermediates} + H^+ \quad (3)$$

Concurrently, the photogenerated electrons accumulated in the conduction band are transferred to titanium-associated surface sites, where they are stabilized and subsequently participate in proton reduction processes occurring mainly at the outer face of the nanotubes: [98]

$$2H^+ + 2e^-\text{CB} \rightarrow H_2 \quad (4)$$

Therefore, the overall reaction can be described as the oxidative breakdown of TEOA coupled with the reduction of protons into molecular hydrogen: [96]

$$TEOA + H_2O \rightarrow (h\nu, \text{Ti-Imogolite}) \text{ oxidized products} + H_2 \quad (5)$$

The photogenerated charge carriers generated in Equation (1) induce the adsorption and oxidation of the sacrificial electron provider, leading to effective hole scavenging and suppressing electron–hole recombination. In contrast to alcohol-based sacrificial agents, TEOA offers multiple oxidation routes and a continuous supply of protons, which augments hydrogen evolution effectiveness. The oxidation processes are expected to happen preferentially within the inner cavities and on the inner exteriors of the nanotubes, where TEOA molecules can be confined and strongly interact with photogenerated holes. Conversely, the reduction of protons to hydrogen molecules is favored on the outer surface of the Ti/Ge nanotubes, where titanium sites promote electron localization and transfer. This spatial separation between oxidation and reduction reactions further contributes to improved charge separation and higher hydrogen output values. The combined influences of effective hole scavenging, titanium-mediated electron trapping, and the one-dimensional nanotubular structure ultimately account for the superior photocatalytic performance observed in the presence of TEOA.

Table 1: Photocatalytic hydrogen production rates for pristine Imogolite and Ti-Imogolite under various experimental conditions, including different sacrificial agents, concentrations, light sources, distances, and stirring speeds.

H_2 production rate (μmol g^{-1} h^{-1}) Ti-Imogolite	**H_2 production rate (μmol g^{-1} h^{-1}) Imogolite**	**Stirring speed (rpm)**	**Light–reactor distance (cm)**	**Light source**	**Solvent concentration**	**Solvent type**	**Experiment No.**
388	57	600	10	UV	10%	MeOH	1
364	42	600	10	UV	10%	EtOH	2
415	73	600	10	UV	10%	TEOA	3
403	61	600	10	UV	5%	TEOA	4
415	73	600	10	UV	10%	TEOA	5
398	68	600	10	UV	20%	TEOA	6
415	73	600	10	UV	10%	TEOA	7
377	46	600	10	Solar simulator	10%	TEOA	8
442	85	600	5	UV	10%	TEOA	9
415	73	600	10	UV	10%	TEOA	10
409	64	600	15	UV	10%	TEOA	11
431	71	300	5	UV	10%	TEOA	12
442	85	600	5	UV	10%	TEOA	13
470	96	900	5	UV	10%	TEOA	14

II -3-2 **Radical Scavenger Tests**

The influence of radical scavengers on photocatalytic hydrogen generation under optimized conditions is summarized in Table 2, offering direct insight into the nature of the active charge carriers and reactive species involved in the photocatalytic process. In the absence of any scavenger, hydrogen evolution rates of 96 and 470 μmol g^{-1} h^{-1} are attained for Imogolite and Ti-Imogolite, respectively, serving as reference values for assessing the effect of selective trapping agents. Upon introduction of benzoquinone (BQ), a recognized superoxide radical ($\bullet O_2^-$) scavenger, the hydrogen evolution speed decreases moderately to 85 μmol g^{-1} h^{-1} for Imogolite

and 420 µmol g^{-1} h^{-1} for Ti-Imogolite. This partial inhibition suggests that •O_2^- species participate in the photocatalytic procedure but do not constitute the main pathway for hydrogen evolution. When isopropanol (IPA), a hydroxyl radical (•OH) scavenger, is applied, only a slight decrease in hydrogen generation is noted, with figures of 90 and 445 µmol g^{-1} h^{-1} for Imogolite and Ti-Imogolite, correspondingly, showing that •OH radicals play a minor role in the hydrogen release reaction. Conversely, the introduction of EDTA, a hole (h^+) scavenger, leads to a marked reduction in hydrogen evolution, decreasing the activity to 60µmol g^{-1} h^{-1} for Imogolite and 300 µmol g^{-1} h^{-1} for Ti-Imogolite. This substantial suppression underscores the vital function of photogenerated holes in sustaining high hydrogen evolution rates by preventing electron–hole recombination. The most pronounced decrease in hydrogen release seen upon the addition of $AgNO_3$, an electron quencher, where the hydrogen output rate decreases sharply to 25 µmol g^{-1} h^{-1} for Imogolite and 110 µmol g^{-1} h^{-1} for Ti-Imogolite, directly verifying that photogenerated electrons are the principal active species responsible for hydrogen evolution. Throughout all scavenger trials, Ti-Imogolite consistently exhibits greater hydrogen release speeds than native Imogolite, implying that titanium insertion improves charge carrier separation and stabilizes photogenerated electrons against scavenging effects. In summary, the findings presented in Table 2 clearly indicate that photocatalytic hydrogen generation in this system is predominantly dictated by conduction-band electrons, with photogenerated holes playing an essential secondary role, while radical species such as •O_2^- and •OH contribute only slightly [100].

Table 2: Effect of radical scavengers on photocatalytic hydrogen generation under optimized conditions

Scavenger	H_2 production rate ($\mu mol\ g^{-1}\ h^{-1}$) Imogolite	H_2 production rate ($\mu mol\ g^{-1}\ h^{-1}$) Ti-Imogolite
None (Blank)	96	470
BQ ($\bullet O_2^-$ scavenger)	85	420
IPA (•OH scavenger)	90	445
EDTA (h^+ scavenger)	60	300
$AgNO_3$ (e^- scavenger)	25	110

II -3-3 Recycling Performance of Imogolite and Ti-Imogolite

The recycling performance of the photocatalysts was systematically assessed under the optimized hydrogen generation conditions, and the corresponding hydrogen evolution rates over five consecutive cycles are summarized in Table 2. Ti-Imogolite displays notable photocatalytic stability, as the hydrogen production rate decreases only slightly from 470 µmol g^{-1} h^{-1} in the first cycle to 467, 460, 459, and 455 µmol g^{-1} h^{-1} in the second to fifth cycles, respectively. This corresponding to an activity retention of over 96% after five cycles, indicating that the Ti-modified material preserves both its structural integrity and catalytic activity during extended operation. In contrast, pristine Imogolite shows a more significant decline in activity upon recycling, with hydrogen evolution decreasing from 96 µmol g^{-1} h^{-1} in the first cycle to 90, 85, 81, and 77µmol g^{-1} h^{-1} over subsequent cycles, corresponding to an activity retention of approximately 80%. The faster deactivation seen for pristine Imogolite can be ascribed to less efficient charge separation and a greater likelihood of surface recombination events during repeated illumination, which progressively diminish the availability of active sites for proton reduction. The superior recyclability of Ti-Imogolite underscores the reinforcing role of titanium incorporation, which not only boosts initial photocatalytic activity but also refines charge carrier handling by capturing photogenerated electrons and reducing recombination losses. Furthermore, the presence of titanium-related electronic states is anticipated to promote more efficient electron-transfer pathways and protect surface active sites from photocorrosion or surface restructuring during repeated cycles. The slight decrease in activity observed for Ti-Imogolite

thus proves that titanium modification successfully enhances both the operational stability and long-term durability of the photocatalyst, verifying its suitability for continuous photocatalytic hydrogen generation [99].

Table 3: Recycling performance of Imogolite and Ti-Imogolite

Cycle number	H_2 production rate ($\mu mol\ g^{-1}\ h^{-1}$) Imogolite	H_2 production rate ($\mu mol\ g^{-1}\ h^{-1}$) Ti-Imogolite
1st cycle	96	470
2nd cycle	90	467
3rd cycle	85	460
4th cycle	81	459
5th cycle	77	455

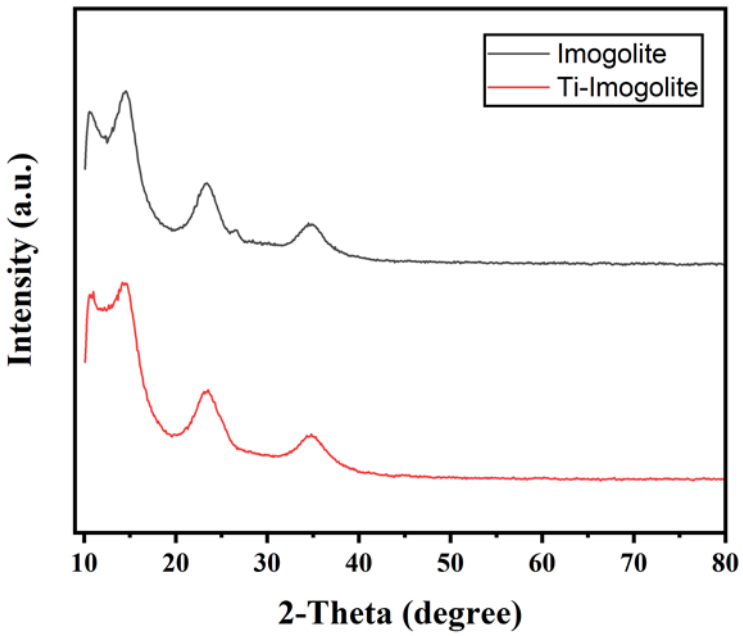

Figure 7: Post-reaction XRD analysis of Ti-Imogolite nanotubes after 5 cycles of hydrogen evolution.

Conclusion

Conclusion

This study demonstrates a comprehensive investigation of photocatalytic hydrogen generation employing titanium-modified Imogolite nanotubes, with a particular focus on the systematic optimization of reaction parameters controlling hydrogen evolution. The controlled hydrothermal synthesis allowed for the successful integration of titanium inside the Imogolite structure while preserving the characteristic tubular morphology.

Beyond the material formulation, an systematic optimization study was conducted to pinpoint the most significant experimental conditions influencing photocatalytic performance. The results clearly show that hydrogen evolution is highly reliant on the reaction conditions. Among the sacrificial agents tested, triethanolamine (TEOA) showed the most effective hole-scavenging ability, showing an ideal concentration of 10%. Moreover, increasing photon flux by decreasing the lamp–reactor distance and improving mass transfer via higher stirring speeds substantially boosted hydrogen output.

Under the refined settings 10% TEOA, UV illumination, a lamp–reactor distance of 5 cm, and an agitation rate of 900 rpm the Ti-Imogolite photocatalyst reached a hydrogen evolution rate of 470 $\mu mol\ g^{-1}\ h^{-1}$, signifying almost a fivefold increase compared with pristine Imogolite. Mechanistic studies suggested that this advance stems from titanium-induced electronic states that encourage effective charge separation and electron transfer.

This research proves that the combined effect of material design and systematic reaction optimization is vital for maximizing photocatalytic hydrogen generation. The discoveries not only emphasize the capability of Ti-modified Imogolite nanotubes as promising photocatalysts but also offer useful guidelines for optimizing photocatalytic systems toward better solar-to-hydrogen energy transformation.

References

References

[1] S. A. Ansari, “Sustainable hydrogen production: Review of methods and technologies,” Glob. Challenges, 2025.

[2] M. A. Rasool, “An insight into carbon nanomaterial-based photocatalytic water splitting for green hydrogen production,” Energies, vol. 19, no. 1, article 59, 2026.

[3] B. Oussmou, “A review on green hydrogen production via water electrolysis: Challenges and perspectives,” Energy Environ. Sci., vol. 7, pp. 395–411, 2014.

[4] J. Smith, “Photocatalytic water splitting: Progress and challenges,” Renew. Sustain. Energy Rev., vol. 211, p. 112768, 2024.

[5] Maryam, “Semiconductor nanomaterial photocatalysts for water-splitting hydrogen production,” J. Mater. Chem. A, vol. 11, no. 23, pp. 11042–11068, 2023.

[6] X. Chen, “2D materials for enhanced photocatalytic hydrogen generation,” ACS Energy Lett., vol. 4, no. 10, pp. 2370–2380, 2019.

[7] E. Paineau, G. Teobaldi, and P. Jiménez-Calvo, “Imogolite nanotubes and their permanently polarized bifunctional surfaces for photocatalytic hydrogen production,” 2024.

[8] P. Jiménez-Calvo, “Ti-modified Imogolite nanotubes as promising photocatalyst 1D nanostructures for H2 production,” Small Methods, vol. 8, no. 8, 2024.

[9] P. Jiménez-Calvo, “Experimental insights into Ti-incorporated Imogolite nanotubes for enhanced photocatalytic activity,” 2024.

[10] R. Li et al., “A review of efficient photocatalytic water splitting for hydrogen production,” Renew. Sustain. Energy Rev., vol. 206, p. 114863, 2024.

[11] Q. Wang and K. Domen, “Particulate Photocatalysts for Light-Driven Water Splitting: Mechanisms, Challenges, and Design Strategies,” Chem. Rev., vol. 120, no. 2, pp. 919–985, 2020.

[12] M. A. Green, K. Emery, Y. Hishikawa, and W. Warta, “Solar cell efficiency tables (Version 57),” Prog. Photovoltaics Res. Appl., vol. 28, no. 1, pp. 3–15, 2020.

[13] Wada, K., & Yoshinaga, N. (1969). The structure of “Imogolite”. American Mineralogist: Journal of Earth and Planetary Materials, 54(1-2), 50-71.

[14] Cradwick, P. D. G., Farmer, V. C., Russell, J. D., Masson, C. R., Wada, K., & Yoshinaga, N. (1972). Imogolite, a hydrated aluminium silicate of tubular structure. Nature Physical Science, 240(104), 187-189.

[15] Farmer, V. C., Fraser, A. R., Russell, J. D., & Yoshinaga, N. (1977). Recognition of Imogolite structures in allophanic clays by infrared spectroscopy. Clay Minerals, 12(1), 55-57.

[16] Parfitt, R. L. (2009). Allophane and imogolite: role in soil biogeochemical processes. Clay minerals, 44(1), 135-155.

[17] Govan, J., Arancibia-Miranda, N., Escudey, M., Bonelli, B., & Tasca, F. (2021). Imogolite: a nanotubular aluminosilicate: synthesis, derivatives, analogues, and general and biological applications. Materials Chemistry Frontiers, 5(18), 6779-6802.

[18] Yoshinaga, N., & Aomine, S. (1962). Allophane in some Ando soils. Soil science and plant nutrition, 8(2), 6-13.

[19] Wada, K. (1967). A structural scheme of soil allophane. American Mineralogist: Journal of Earth and Planetary Materials, 52(5-6), 690-708.

[20] Bursill, L. A., Peng, J. L., & Bourgeois, L. N. (2000). Imogolite: an aluminosilicate nanotube material. Philosophical Magazine A, 80(1), 105-117.

[21] d'Angelo, A., Paineau, E., Rouzière, S., Elkaim, É., Goldmann, C., Toquer, D., ... & Launois, P. (2023). The atomic structure of Imogolite nanotubes: A 50 years old issue reinvestigated by X-ray scattering experiments and molecular dynamics simulations. Applied Clay Science, 242, 107043.

[22] Guimarães, L., Enyashin, A. N., Frenzel, J., Heine, T., Duarte, H. A., & Seifert, G. (2007). Imogolite nanotubes: stability, electronic, and mechanical properties. Acs Nano, 1(4), 362-368.

[23] Koji, W. (1989). Allophane and Imogolite. Minerals in soil environments, 1, 1051-1087.

[24] Thill, A. (2016). Characterisation of imogolite by microscopic and spectroscopic methods. In P. Yuan, A. Thill, & F. Bergaya (Eds.), Nanosized tubular clay minerals: Halloysite and Imogolite (pp. 223–253). Elsevier.

[25] Fernandez-Martinez, A., Tao, J., Wallace, A. F., Bourg, I. C., Johnson, M. R., De Yoreo, J. J., ... & Charlet, L. (2020). Curvature-induced hydrophobicity at Imogolite–water interfaces. Environmental Science: Nano, 7(9), 2759-2772.

[26] Du, P., Yuan, P., Thill, A., Annabi-Bergaya, F., Liu, D., & Wang, S. (2017). Insights into the formation mechanism of Imogolite from a full-range observation of its sol-gel growth. Applied Clay Science, 150, 115-124.

[27] Scalfi, L., Fraux, G., Boutin, A., & Coudert, F. X. (2018). Structure and dynamics of water confined in Imogolite nanotubes. Langmuir, 34(23), 6748-6756.

[28] Paineau, E., & Launois, P. (2019). Nanomaterials from Imogolite: structure, properties, and functional materials. In Nanomaterials from clay minerals (pp. 257-284). Elsevier.

[29] Guggenheim, S., Pasbakhsh, P., & Churchman, G. J. (2015). Phyllosilicates used as nanotube substrates in engineered materials: structures, chemistries, and textures. Natural Mineral Nanotubes, 4-48.

[30] Liao, Y., Picot, P., Lainé, M., Brubach, J. B., Roy, P., Thill, A., & Le Caër, S. (2018). Tuning the properties of confined water in standard and hybrid nanotubes: An infrared spectroscopic study. Nano Research, 11(9), 4759-4773.

[31] Pan, Y. H., Zhao, Q. Y., Gu, L., & Wu, Q. Y. (2017). Thin film nanocomposite membranes based on Imologite nanotubes blended substrates for forward osmosis desalination. Desalination, 421, 160-168.

[32] Li, M., & Brant, J. A. (2018). Synthesis of polyamide thin-film nanocomposite membranes using surface modified imogolite nanotubes. Journal of Membrane Science, 563, 664-675.

[33] Gelli, R., Del Buffa, S., Tempesti, P., Bonini, M., Ridi, F., & Baglioni, P. (2018). Enhanced formation of hydroxyapatites in gelatin/Imogolite macroporous hydrogels. Journal of colloid and interface science, 511, 145-154.

[34] Obata, A., Mori, K., Inukai, K., Kato, K., Poologasundarampillai, G., & Kasuga, T. (2020). Three-dimensional cotton-wool-like polyhydroxybutyrate/siloxane-doped vaterite composite fibrous scaffolds: effect of Imogolite-coating on physicochemical and cell adhesion properties. Frontiers in Materials, 7, 33.

[35] Wong, L. W., Goh, C. B. S., Pasbakhsh, P., & Tan, J. B. L. (2022). Natural hollow clay nanotubes and their applications as polymer nanocomposites in tissue engineering. Journal of Science: Advanced Materials and Devices, 7(2), 100431.

[36] Ma, W., Yah, W. O., Otsuka, H., & Takahara, A. (2012). Surface functionalization of aluminosilicate nanotubes with organic molecules. Beilstein journal of nanotechnology, 3(1), 82-100.

[37] da Silva, M. C., dos Santos, E. C., Lourenço, M. P., Gouvea, M. P., & Duarte, H. A. (2015). Structural, electronic, and mechanical properties of inner surface modified Imogolite nanotubes. Frontiers in Materials, 2, 16.

[38] Moreno-Rodríguez, D., Gianni, E., Pospíšil, M., & Scholtzová, E. (2023). Is Imogolite a suitable adsorbent agent for the herbicides like diuron and atrazine?. Journal of Molecular Liquids, 380, 121732.

[39] Callister Jr, W. D., & Rethwisch, D. G. (2020). Materials science and engineering: an introduction. John wiley & sons.

[40] Cullity, B. D., & Stock, S. R. (2001). Elelments of X-ray Diffraction. Prentice-Hall.

[41] Smith, B. C. (2011). Fundamentals of Fourier transform infrared spectroscopy. CRC press.

[42] Leng, Y. (2013). Materials characterization: introduction to microscopic and spectroscopic methods. John Wiley & Sons.

[43] Goldstein, J. I., Newbury, D. E., Michael, J. R., Ritchie, N. W., Scott, J. H. J., & Joy, D. C. (2017). Scanning electron microscopy and X-ray microanalysis. springer.

[44] Jenkins, R. (1999). X-ray fluorescence spectrometry (Vol. 152, pp. 101-107). New York: Wiley.

[45] George, G., Wilson, R., & Joy, J. (2017). Ultraviolet spectroscopy: a facile approach for the characterization of nanomaterials. In Spectroscopic methods for nanomaterials characterization (pp. 55-72). Elsevier.

[46] Mäntele, W., & Deniz, E. (2017). UV–VIS absorption spectroscopy: Lambert-Beer reloaded. Spectrochimica Acta Part A: Molecular and Biomolecular Spectroscopy, 173, 965-968.

[47] Tauc, J., & Menth, A. (1972). States in the gap. Journal of non-crystalline solids, 8, 569-585.

[48] TEREA, H. (2023). Application of cellulose/ZnO nanocomposite on the removal of toxic pollutants from aqueous solutions (Doctoral dissertation).

[49] de Viguerie, L. (2009). Propriétés physico-chimiques et caractérisation des matériaux du ‘sfumato' (Doctoral dissertation, Université Pierre et Marie Curie-Paris VI).

[50] GUERRAM, A. (2022). Synthèse verte et caractérisation des nanoparticules de ZnO à l’aide d’extrait des feuilles de Phoenix dactylifera L et leur applications (Doctoral dissertation, Faculté des Sciences et de la technologie).

[51] Serna, F., Lagneau, J., & Carpentier, J. M. (2014). La diffraction des rayons X: une technique puissante pour résoudre certains problèmes industriels et technologiques. Chim. Nouv, 1-12.

[52] Ghidan, A. Y., Al-Antary, T. M., & Awwad, A. M. (2016). Green synthesis of copper oxide nanoparticles using Punica granatum peels extract: Effect on green peach Aphid. Environmental Nanotechnology, Monitoring & Management, 6, 95-98.

[53] Megashah, L. N., Ariffin, H., Zakaria, M. R., Hassan, M. A., Andou, Y., & Padzil, F. N. M. (2020). Modification of cellulose degree of polymerization by superheated steam treatment for versatile properties of cellulose nanofibril film. Cellulose, 27(13), 7417-7429.

[54](كودية و سماحي ، دراسة الخصائص الفيزيو كيميائية للرماد الناتج عن حرق النفايات الخطرة * دراسة حالة : مؤسسة ترانس كو بورقلة * (رسالة ماجستير)، 2025)

[55]لمواد بناء قصر تاجموت (XRF) بوهدة, آمال, عيساوي, & بوعكاز. (2024). التحليل بتقنية الفلورة بالأشعة السينية بالأغواط. مجلة العلوم القانونية والاجتماعية, 9(2), 477-497.

[56] PAQUETON, H., & RUSTE, J. (2006). Microscopie électronique à balayage Principe et équipement. Techniques de l'ingénieur. Analyse et caractérisation, (P865v2).

[57] Ben Mya, O. (2015). Synthèse et caractérisation de la pérovskite La1-x SrxFe0. 7Ni0. 3O3 (Doctoral dissertation, Université Mohamed Khider-Biskra).

[58] Chen, X., Shen, S., Guo, L., & Mao, S. S. (2010). Semiconductor-based photocatalytic hydrogen generation. Chemical Reviews, 110(11), 6503–6570.

[59] Hisatomi, T., Kubota, J., & Domen, K. (2014). Recent advances in semiconductors for photocatalytic and photoelectrochemical water splitting. Chemical Society Reviews, 43(22), 7520–7535.

[60] Lewis, N. S., & Nocera, D. G. (2006). Powering the planet: Chemical challenges in solar energy utilization. Proceedings of the National Academy of Sciences, 103(43), 15729-15735.

[61] Wang, Z., Li, C., & Domen, K. (2019). Recent developments in heterogeneous photocatalysts for solar-driven overall water splitting. Chemical Society Reviews, 48(7), 2109-2125.

[62] Fujishima, A., Zhang, X., & Tryk, D. A. (2008). TiO2 photocatalysis and related surface phenomena. Surface science reports, 63(12), 515-582.

[63] Baly, E. C. C., Heilbron, I. M., & Hudson, D. P. (1922). CXXX.—Photocatalysis. Part II. The photosynthesis of nitrogen compounds from nitrates and carbon dioxide. Journal of the Chemical Society, Transactions, 121, 1078-1088.

[64] Serpone, N., & Pelizzetti, E. (1989). Photocatalysis: fundamentals and applications. (No Title).

[65] Braslavsky, S. E., Braun, A. M., Cassano, A. E., Emeline, A. V., Litter, M. I., Palmisano, L., ... & Serpone, N. (2011). Glossary of terms used in photocatalysis and radiation catalysis (IUPAC Recommendations 2011). Pure and Applied Chemistry, 83(4), 931-1014.

[66] Serpone, N., Emeline, A. V., Horikoshi, S., Kuznetsov, V. N., & Ryabchuk, V. K. (2012). On the genesis of heterogeneous photocatalysis: a brief historical perspective in the period 1910 to the mid-1980s. Photochemical & Photobiological Sciences, 11(7), 1121-1150.

[67] Fujishima, A., & Honda, K. (1972). Electrochemical photolysis of water at a semiconductor electrode. nature, 238(5358), 37-38.

[68] Dincer, I. (2012). Green methods for hydrogen production. International journal of hydrogen energy, 37(2), 1954-1971.

[69] Ursua, A., Gandia, L. M., & Sanchis, P. (2011). Hydrogen production from water electrolysis: current status and future trends. Proceedings of the IEEE, 100(2), 410-426.

[70] Bhandari, R., Trudewind, C. A., & Zapp, P. (2014). Life cycle assessment of hydrogen production via electrolysis–a review. Journal of cleaner production, 85, 151-163.

[71] Laguna-Bercero, M. A. (2012). Recent advances in high temperature electrolysis using solid oxide fuel cells: A review. Journal of Power sources, 203, 4-16.

[72] Nikolaidis, P., & Poullikkas, A. (2017). A comparative overview of hydrogen production processes. Renewable and sustainable energy reviews, 67, 597-611.

[73] Dawood, F., Anda, M., & Shafiullah, G. M. (2020). Hydrogen production for energy: An overview. International journal of hydrogen energy, 45(7), 3847-3869.

[74] Steinfeld, A. (2005). Solar thermochemical production of hydrogen—a review. Solar energy, 78(5), 603-615.

[75] Azwar, M. Y., Hussain, M. A., & Abdul-Wahab, A. K. (2014). Development of biohydrogen production by photobiological, fermentation and electrochemical processes: a review. Renewable and Sustainable Energy Reviews, 31, 158-173.

[76] Schneider, J., Matsuoka, M., Takeuchi, M., Zhang, J., Horiuchi, Y., Anpo, M., & Bahnemann, D. W. (2014). Understanding TiO2 photocatalysis: mechanisms and materials. Chemical reviews, 114(19), 9919-9986.

[77] (خلفاوي، طريلي ، و عريق، الهيدروجين الأخضر (رسالة ماجستير)، 2025)

[78] عباس و وناس ، دراسة نظرية حول تعديل فجوة الطاقة للمحفز الضوئي ثاني أكسيد التيتانيوم باستخدام طريقة التشويب (رسالة الماجستير)، 2021))

[79] زروقي و شعيب ، انتاج الهيدروجين الأخضر كمصدر للطاقة في منطقة ورقلة (رسالة ماجستير)، 2024)

[80] R. Li et al., “A review of efficient photocatalytic water splitting for hydrogen production,” Renew. Sustain. Energy Rev., vol. 206, p. 114863, 2024.

[81] Q. Wang and K. Domen, “Particulate Photocatalysts for Light-Driven Water Splitting: Mechanisms, Challenges, and Design Strategies,” Chem. Rev., vol. 120, no. 2, pp. 919–985, 2020.

[82] M. A. Green, K. Emery, Y. Hishikawa, and W. Warta, “Solar cell efficiency tables (Version 57),” Prog. Photovoltaics Res. Appl., vol. 28, no. 1, pp. 3–15, 2020.

[83] O. Zemali et al., “Citric Acid-Assisted Biosynthesis of MgO/MgO2 Nanocomposites: Enhanced Photocatalytic Degradation of Brilliant Cresyl Blue, Antibacterial and Antioxidant Activity Supported by Computational Simulations,” J. Clust. Sci., vol. 35, no. 8, pp. 2913–2929, 2024.

[84] X. Chen and S. S. Mao, “Titanium dioxide nanomaterials: synthesis, properties, modifications, and applications,” Chem. Rev., vol. 107, no. 7, pp. 2891–2959, 2007.

[85] S. A. Ansari, “Sustainable hydrogen production: Review of methods and technologies,” Glob. Challenges, 2025.

[86] M. A. Rasool, “An insight into carbon nanomaterial-based photocatalytic water splitting for green hydrogen production,” Energies, vol. 19, no. 1, p. 59, 2026.

[87] B. Oussmou, “A review on green hydrogen production via water electrolysis: Challenges and perspectives,” Energy Environ. Sci., vol. 7, pp. 395–411, 2014.

[88] J. Smith, “Photocatalytic water splitting: Progress and challenges,” Renew. Sustain. Energy Rev., vol. 211, p. 112768, 2024.

[89] Maryam, “Semiconductor nanomaterial photocatalysts for water-splitting hydrogen production,” J. Mater. Chem. A, vol. 11, no. 23, pp. 11042–11068, 2023.

[90] P. Picot, Y. Liao, E. Barruet, F. Gobeaux, T. Coradin, and A. Thill, “Exploring hybrid Imogolite nanotube formation via Si/Al stoichiometry control,” Langmuir, vol. 34, no. 44, pp. 13225–13234, 2018.

[91] Y. Zhang et al., “Fast hydrothermal and microwave synthesis of high purity methylated Imogolite nanotubes,” Appl. Clay Sci., vol. 274, p. 107851, 2025.

[92] Y. Liao, P. Picot, J.-B. Brubach, P. Roy, S. Le Caër, and A. Thill, “Self-supporting thin films of Imogolite and Imogolite-like nanotubes for infrared spectroscopy,” Appl. Clay Sci., vol. 164, pp. 58–67, 2018.

[93] P. Jiménez-Calvo, “Ti-modified Imogolite nanotubes as promising photocatalyst 1D nanostructures for H2 production,” Small Methods, vol. 8, no. 8, 2024.

[94] J. D. Elliott et al., “Chemically selective alternatives to photoferroelectrics for polarization-enhanced photocatalysis: the untapped potential of hybrid inorganic nanotubes,” Adv. Sci., vol. 4, no. 2, p. 1600153, 2016.

[95] E. Poli et al., “The potential of Imogolite nanotubes as (co-) photocatalysts: a linear-scaling density functional theory study,” J. Phys. Condens. Matter, vol. 28, no. 7, p. 74003, 2016.

[96] V. Kumaravel, S. Mathew, and S. C. Pillai, “Photocatalytic hydrogen production: Role of sacrificial reagents on the activity of oxide, carbon, and sulfide catalysts,” Catalysts, vol. 9, no. 3, p. 276, 2019.

[97] C. R. Carr, M. A. Vrionides, I. S. Sosulin, A. Lisouskaya, M. Z. Ertem, and D. C. Grills, “Electron transfer theory elucidates the hidden role played by triethylamine and triethanolamine during photocatalysis,” J. Am. Chem. Soc., vol. 147, no. 35, pp. 32005–32014, 2025.

[98] T. Hisatomi, J. Kubota, and K. Domen, “Photocatalytic water splitting: Recent progress and future challenges,” Chem. Soc. Rev., vol. 43, no. 22, pp. 7520–7535, 2014.

[99]A. Kudo and Y. Miseki, “Heterogeneous photocatalyst materials for water splitting,” Chem. Soc. Rev., vol. 38, no. 1, pp. 253–278, 2009.

[100] X. Li, J. Yu, M. Jaroniec, and X. Chen, “Cocatalysts for selective photocatalytic water splitting,” Chem. Rev., vol. 119, no. 6, pp. 3962–4179, 2019.